

Global-mean marine $\delta^{13}\text{C}$ and its uncertainty in a glacial state estimate

Geoffrey Gebbie^a, Carlye D. Peterson^b, Lorraine E. Lisiecki^b, Howard J. Spero^c

^a*Department of Physical Oceanography, Woods Hole Oceanographic Institution, 360 Woods Hole Rd., MS # 29, Woods Hole, MA, 02543 USA, ggebbie@whoi.edu*

^b*Department of Earth Science, University of California, Santa Barbara, California, USA*

^c*Department of Earth and Planetary Sciences, University of California, Davis, California, USA*

Abstract

A paleo-data compilation with 492 $\delta^{13}\text{C}$ and $\delta^{18}\text{O}$ observations provides the opportunity to better sample the Last Glacial Maximum (LGM) and infer its global properties, such as the mean $\delta^{13}\text{C}$ of dissolved inorganic carbon. Here, the paleo-compilation is used to reconstruct a steady-state water-mass distribution for the LGM, that in turn is used to map the data onto a 3D global grid. A global-mean marine $\delta^{13}\text{C}$ value and a self-consistent uncertainty estimate are derived using the framework of state estimation (i.e., combining a numerical model and observations). The LGM global-mean $\delta^{13}\text{C}$ is estimated to be $0.14\text{‰} \pm 0.20\text{‰}$ at the two standard error level, giving a glacial-to-modern change of $0.32\text{‰} \pm 0.20\text{‰}$. The magnitude of the error bar is attributed to the uncertain glacial ocean circulation and the lack of observational constraints in the Pacific, Indian, and Southern Oceans. Observations in the Indian and Pacific Oceans generally have 10 times the weight of an Atlantic point in the computation of the global mean. To halve the error bar, roughly four times more observations are needed, although strategic sampling may reduce this number. If dynamical constraints can be used to better characterize the LGM circulation, the error bar can also be reduced to 0.05 to

0.1‰, emphasizing that knowledge of the circulation is vital to accurately map $\delta^{13}\text{C}_{\text{DIC}}$ in three dimensions.

Keywords: Paleoceanography, Physical Oceanography, Carbon reservoirs, Last Glacial Maximum, Inverse methods

1. Introduction

Carbon-13 to carbon-12 ratios (i.e., $\delta^{13}\text{C}$) can chemically fingerprint different carbon reservoirs, and thus glacial-interglacial changes in $\delta^{13}\text{C}$ of oceanic dissolved inorganic carbon (i.e., $\delta^{13}\text{C}_{\text{DIC}}$) reflect the carbon partitioning between terrestrial, atmospheric, and marine reservoirs. Dramatic environmental changes during the Last Glacial Maximum (LGM, 23,000 to 19,000 years before present) altered the terrestrial biosphere, and some of the low isotopic signature of terrestrial carbon ($\delta^{13}\text{C} \approx -25\text{‰}$) was transferred to the glacial ocean, consistent with observations of benthic foraminiferal $\delta^{13}\text{C}$ lower than the modern-day (e.g., Shackleton, 1977; Curry et al., 1988; Duplessy et al., 1988). The glacial atmosphere held approximately 170 gigatons (Gt) less carbon (e.g., Monnin et al., 2001), leaving the ocean as the most readily available source of compensation for the other two reservoirs. Pollen records and vegetation models that more directly reflect terrestrial carbon change yield higher estimates of glacial-to-modern carbon transfer (e.g., 750 to 1900 Gt C, Crowley, 1995; Adams and Faure, 1998; Kaplan et al., 2002) than the marine-based estimates (e.g., 330 to 650 Gt C, Shackleton, 1977; Curry et al., 1988; Duplessy et al., 1988; Köhler et al., 2010), although an inert terrestrial carbon pool may reconcile the difference (Ciais et al., 2012). A recent compilation of benthic *Cibicidoides* spp. $\delta^{13}\text{C}$ has nearly twice the data points of previous compilations and coverage of the Atlantic, Pacific, and

21 Indian Oceans (Peterson et al., 2014), and thus motivates the re-investigation of
22 the marine-based whole-ocean $\delta^{13}\text{C}$ estimates.

Determining the mean value of a spatially-distributed tracer field reduces to a linear operation in most cases (i.e., an inner vector product):

$$\bar{c} = \mathbf{w}^T \mathbf{y} + \bar{c}_0 = \sum_{i=1}^N w_i y_i + \bar{c}_0 \quad (1)$$

23 where \bar{c} is the global mean value of a tracer c , \mathbf{w} is a vector of weights with w_i for
24 the i th element, T is the vector transpose, \mathbf{y} is a vector containing N observations of
25 y_i , and \bar{c}_0 is a constant included for full generality. If all observations are assumed
26 to contain equal information about the global mean and no other information is
27 available (i.e., $\bar{c}_0 = 0$), the optimal weights would all be $1/N$, and equation (1)
28 reverts to the basic sample mean. The sparse, irregularly-spaced nature of glacial
29 observations invalidates this assumption, of course. Originally, paleoceanogra-
30 phers best dealt with this issue by choosing cores from what was thought to be
31 the most representative oceanic regions (e.g., Shackleton, 1977). As more data
32 became available, basin-wide or regional means were computed as a preliminary
33 step before global averaging (e.g. Curry et al., 1988; Boyle, 1992; Matsumoto and
34 Lynch-Stieglitz, 1999; Peterson et al., 2014). This multi-step process naturally
35 leads to non-uniform weights on the observations in equation (1).

36 When the global-mean oceanic $\delta^{13}\text{C}_{\text{DIC}}$ is computed as a succession of sub-
37 averages, the result may be sensitive to the size and location of the chosen sub-
38 domains, and only by producing $\delta^{13}\text{C}$ maps at higher spatial resolution will this
39 sensitivity be reduced. The distance between LGM observations, however, is often
40 greater than the decorrelation lengthscale of oceanic property fields, and thus the
41 typical method of “objectively” mapping the observations onto a regular grid (e.g.,
42 optimal interpolation or objective mapping, Bretherton et al., 1976) reverts to a

43 first-guess estimate in many locations. In other words, large regions of the LGM
44 ocean would be unconstrained by the data, especially at intermediate depths where
45 little core coverage is available. Furthermore, the objectively-mapped estimate
46 will leave local extrema in the estimated tracer field around the data points. Such
47 features are undesirable because they are not physically sustainable in equilibrium
48 when diffusion has sufficient time to act (e.g., for atmospheric momentum, Hide,
49 1969). It is not clear, however, how equilibrated the glacial ocean was and whether
50 eddy processes can be accurately modeled as a diffusive process. Computation
51 of an accurate global mean is challenging even for modern-day cases, such as
52 sealevel rise (e.g., Wunsch et al., 2007). A new method is needed to create a map
53 with sparse LGM observations that addresses these complications.

54 Here we suggest that a method originally developed for estimating the oceanic
55 water-mass distribution from sparse observations (Gebbie, 2014) is also well-
56 suited to make three-dimensional global maps. Specifically, we combine a tracer
57 transport model (Section 2.1) with observations (Section 2.2) to produce an LGM
58 state estimate. Rather than using the assumed statistics of circulation length-
59 scales, like optimal interpolation, we illustrate that the circulation itself can be
60 used to make a gridded field (Section 2.3). The numerical model serves a dual
61 purpose: 1) a means to readily interpret the sources, sinks, and pathways of tracer,
62 and 2) a kinematic interpolator and extrapolator that allows large-scale informa-
63 tion to be extracted from the observations. Here we extend the state estimation
64 framework by deriving a self-consistent formula for the global-mean uncertainty
65 (Section 2.4).

66 This work has two major results: 1) an estimate of the LGM global-mean
67 $\delta^{13}\text{C}_{\text{DIC}}$, and 2) its uncertainty within a explicit set of assumptions. To connect

88 these results to deglacial climate dynamics and the carbon cycle, we reconstruct
89 a global map of LGM $\delta^{13}\text{C}_{\text{DIC}}$ and detect a largescale, coherent pattern of LGM-
90 to-modern changes (Section 3). The glacial-mean $\delta^{13}\text{C}_{\text{DIC}}$ uncertainty is partially
91 attributed to the sparsity and measurement error in the observations, but also due to
92 the difficulty in accurately modeling the LGM circulation (Section 4). Our results
93 are discussed in the context of previous observational techniques (Section 5), es-
94 pecially how the observational weights in the averaging equation (1) are modified
95 by the assumed circulation regime. We conclude by emphasizing the importance
96 of circulation knowledge in the goal of further reducing the global-mean $\delta^{13}\text{C}_{\text{DIC}}$
97 uncertainty (Section 6).

78 **2. Global LGM state estimate**

79 The global LGM state estimate is produced by combining a kinematic tracer
80 transport model with a global array of benthic foraminiferal observations of $\delta^{13}\text{C}$
81 and $\delta^{18}\text{O}$. Global, three-dimensional gridded distributions are produced for mul-
82 tiple tracers: $\delta^{13}\text{C}_{\text{DIC}}$, seawater $\delta^{18}\text{O}$ (i.e., $\delta^{18}\text{O}_w$), potential temperature, practical
83 salinity, and phosphate. The model, observations, and state estimation method are
84 detailed next.

85 *2.1. Model*

86 The model is a statistically steady-state conservation equation that is assumed
87 to hold for, C , a general tracer: $\nabla \cdot (\vec{F}C) = Q$, where \vec{F} is the mass flux and Q is
88 a local source or sink. In the statistical steady state, any temporal variability that
89 has a net diffusive or advective effect is represented by the model used here.

In practice, the model equations are discretized on a global, three-dimensional
grid. Here the grid is defined with $4^\circ \times 4^\circ$ horizontal resolution and 33 vertical

levels with enhanced resolution near the surface. Glacial ocean computations are undertaken on the same grid as a modern-day reference case, but gridcells shallower than 120 meters modern-day water depth are discarded due to the sealevel drop. After discretization, the equations are normalized by the sum of all mass fluxes into the gridcell, $\phi_i = \sum_{j=1}^N f_{ij}$, where f_{ij} is the flux from gridcell j to i , and there are N neighboring gridcells. Then the tracer transport equation at gridcell i becomes more similar to a water-mass mixing model (following Gebbie and Huybers, 2012):

$$\sum_{j=1}^N m_{ij}c_j - c_i = q_i \quad (2)$$

90 where m_{ij} is the ratio of the inward flux from j to the total flux ($m_{ij} = f_{ij}/\phi_i$), c_i is
 91 the tracer concentration in cell i , and q_i is equilibrium tracer source with units of
 92 the tracer concentration itself ($q_i = Q/\phi_i$). For conservative tracers, the source and
 93 sink vanishes ($Q = 0$). These algebraic manipulations lead to a well-conditioned
 94 set of equations that can be solved quickly, but with the tradeoff that information
 95 is lost regarding the absolute rate of circulation.

96 The isotope variables, $\delta^{13}\text{C}_{\text{DIC}}$ and $\delta^{18}\text{O}_w$, require some further consideration.
 97 In particular, the sink of $\delta^{13}\text{C}_{\text{DIC}}$ due to remineralization is assumed to be equal
 98 to $-0.95\text{‰}/(\mu\text{mol/kg})$ times the source of remineralized phosphate, which is ad-
 99 justed relative to the modern ratio of $-1.1\text{‰}/(\mu\text{mol/kg})$ due to changes in whole-
 100 ocean $\delta^{13}\text{C}_{\text{DIC}}$ and upper-ocean biological fractionation (e.g., following Broecker
 101 and Maier-Reimer, 1992). Here we model the ratio (delta value) rather than the in-
 102 dividual isotopes which incurs an error (e.g., Walker, 1991), but it is small because
 103 the $^{18}\text{O}/^{16}\text{O}$ ratio in Vienna Standard Mean Ocean Water (VSMOW) standard is
 104 about 1/500, and the $^{13}\text{C}/^{12}\text{C}$ ratio in the Vienna Pee Dee Belemnite (VPDB)
 105 standard is about 1/90. Furthermore, this error is damped in the vicinity of obser-

106 vations by the formal data constraints.

107 For reasons that should become clear below, the state vector, \mathbf{x} , is defined to
108 contain both tracer and circulation information, i.e., $\mathbf{x}^T = [\mathbf{c}; \mathbf{m}]^T$, where \mathbf{c} is a
109 vector that represents all of the global three-dimensional tracer distributions and
110 \mathbf{m} describes the circulation by concatenating all of the mass-flux ratios, m_{ij} (e.g.,
111 Gebbie and Huybers, 2010). This state vector definition is not unique, but it pro-
112 vides sufficient information to permit a steady-state tracer distribution to be com-
113 puted, and thus is an acceptable definition of the state. All of the tracer transport
114 equations are combined and symbolically represented as: $\mathcal{L}[\mathbf{x}] = \mathbf{q} + \mathbf{v}$, where \mathcal{L}
115 is a nonlinear operator due to the multiplication of the tracer concentration and
116 flow field that encapsulates advective and diffusive processes, and \mathbf{v} is the source
117 deviation from the modern-day first-guess field, \mathbf{q} . The model equation includes
118 surface concentration (i.e., Dirichlet) boundary conditions for completeness.

119 2.2. Observations

120 A major extension to the work of Gebbie (2014) is the use of the paleo-data
121 compilation of Peterson et al. (2014) that includes observations in the Pacific and
122 Indian sectors, rather than the Atlantic-only data used previously. This compi-
123 lation contains 376 $\delta^{13}\text{C}$ and 369 $\delta^{18}\text{O}$ measurements from benthic foraminifera
124 dated to the Last Glacial Maximum from 23,000 to 19,000 years before present
125 (23-19 kyr BP) following a re-derived age model for many cores (Stern and Lisiecki,
126 2014). The need for inter-species and interlaboratory offsets is reduced by com-
127 piling only *Cibicidoides* spp. $\delta^{13}\text{C}$ data, although there are few data of this type
128 in intermediate waters. Other data are added (e.g., personal communication, D.W.
129 Oppo and W. Curry, Marchal and Curry, 2008; Makou et al., 2010; Hesse et al.,
130 2011), including porewater salinity and $\delta^{18}\text{O}$ data points (Adkins et al., 2002).

131 The deglacial records indicate a group of outliers where the LGM-to-Holocene
132 $\delta^{18}\text{O}$ change is less than 0.6‰ and can be traced to low temporal resolution in the
133 cores. Therefore we have removed these values from the compilation. Observa-
134 tions were also culled when the phytodetritus effect was implicated by the original
135 authors (e.g., Mackensen et al., 2000) and at locations that fall more than 200 km
136 outside of the model grid. When combining the Peterson et al. (2014) compilation
137 with the additional data, we have 492 LGM $\delta^{13}\text{C}$ and 492 $\delta^{18}\text{O}$ data points that
138 constrain the model simulation (locations are later shown in Figure 8).

139 The collection of observational equations is expressed as one matrix equation:
140 $\mathbf{y} = \mathbf{E}\mathbf{x} + \mathbf{n}$, where \mathbf{y} is a vector of observations, \mathbf{E} predicts the observations from
141 the state, \mathbf{x} , and \mathbf{n} is the observational error. We assume that benthic foraminiferal
142 $\delta^{13}\text{C}$ reflects $\delta^{13}\text{C}_{\text{DIC}}$ (e.g., Duplessy et al., 1984) and that the error in this as-
143 sumption is normally distributed with a standard deviation of 0.2‰ (Marchal and
144 Curry, 2008). We check this assumption by calculating the misfit between the
145 Late Holocene core data and a projection of the modern-day $\delta^{13}\text{C}_{\text{DIC}}$ distribution of
146 Gebbie (2014) onto the core sites. The standard deviation of the misfit is 0.27‰,
147 suggesting that 0.2‰ is a reasonable guess of this unknown quantity. Systematic
148 errors in this relationship will be addressed in Section 4.6.

149 2.3. State estimation method

The solution method is started with prior knowledge of the state as encapsulated in a first guess, \mathbf{x}_0 . Here we use modern-day property distributions, but where $\delta^{18}\text{O}_w$ and practical salinity are adjusted higher by 1.1‰ and 1.1 on the practical salinity scale, respectively, to account for glacial sealevel drop. The first-guess constraint is equivalently written as an equation: $\mathbf{x} = \mathbf{x}_0 + \mathbf{u}$, where \mathbf{u} is a deviation from the first guess that is permitted to be large (see the weight matrices

below). Then, the solution state is determined by minimizing a cost function that combines the constraints from this and the previous two sections (2.1 and 2.2)

$$J = \mathbf{u}^T \mathbf{S}^{-1} \mathbf{u} + \mathbf{n}^T \mathbf{W}^{-1} \mathbf{n} + \mathbf{v}^T \mathbf{Q}^{-1} \mathbf{v}, \quad (3)$$

150 where \mathbf{S} , \mathbf{W} , and \mathbf{Q} are matrices that provide the relative weightings (see Ap-
 151 pendix A for the chosen values relevant for equation 3). The three terms on the
 152 right hand side represent the three major constraints: 1) prior information about
 153 the tracer distribution and circulation, 2) proxy observations, and 3) the tracer
 154 transport model.

155 The complete solution method for the global $\delta^{13}\text{C}_{\text{DIC}}$ distribution was reported
 156 by Gebbie (2014) and includes a number of other constraints (and, hence, terms in
 157 the cost function), such as gravitational stability and the non-negativity of tracer
 158 concentrations. To recap, this weighted, tapered least-squares problem is solved
 159 by transforming equation (3) into a constrained cost function by appending La-
 160 grange multiplier terms, and then hand-coding the adjoint equations that give
 161 sensitivity information. It is solved iteratively using a limited-memory quasi-
 162 Newton gradient descent routine (Nocedal, 1980). After solving for the $\delta^{13}\text{C}_{\text{DIC}}$
 163 state, we seek a formula for the global-mean uncertainty that is valid in the neigh-
 164 borhood of the known solution. The final solution is gravitationally stable and
 165 has non-negative tracer distributions, indicating that the additional cost function
 166 terms are not actively constraining the solution at the final iteration. Thus we sim-
 167 plify the uncertainty problem by assuming that equation (3) represents all active
 168 constraints, and derive an uncertainty formula under such an assumption next.

169 *2.4. Global-mean uncertainty of the state estimate*

170 Many methods for computing error bars are available, and we explicitly define
 171 what is meant by uncertainty in this work by following the development of Wunsch
 172 (1996). The uncertainty, $P_{\bar{c}}$, is defined as the expected squared difference between
 173 the estimated global mean, \tilde{c} , and the true value, \bar{c} (i.e., $P_{\bar{c}} \equiv \langle (\tilde{c} - \bar{c})^2 \rangle$),
 174 where the brackets indicate the expected value operator. For an unbiased estimator,
 175 the true solution, \bar{c} , may be set equal to the expected value that would emerge
 176 from our estimation method over many different realizations, $\langle \tilde{c} \rangle$, but here we
 177 restrain from such an interpretation given the highly nonlinear nature of the problem
 178 and the simplified nature of the model. Thus we are restricted to solving
 179 for the expected range of solutions, here defined as the dispersion of \tilde{c} — $\langle \tilde{c} \rangle$
 180 or equivalently the covariance of the global mean, $C_{\bar{c}} \equiv \langle (\tilde{c} - \langle \tilde{c} \rangle)^2 \rangle$. The
 181 standard error, $\sigma_{\bar{c}}$, is then defined as the square root of the solution covariance:
 182 $\sigma_{\bar{c}} \equiv \sqrt{C_{\bar{c}}}$. We follow the convention of Peterson et al. (2014) by quoting twice the
 183 standard error as our estimate of the glacial-mean $\delta^{13}\text{C}_{\text{DIC}}$ uncertainty, which can
 184 naturally be interpreted as the 95% confidence interval of a normally-distributed
 185 process.

Before calculating the uncertainty of the global mean, we first define the global mean explicitly as

$$\bar{c} = \mathbf{r}^T \mathbf{x}, \quad (4)$$

186 where \mathbf{r} is the appropriately-defined mass-weighting vector (i.e., $r_i = M_i / \sum_{j=1}^J M_j$
 187 for all $i \leq J$ where M_i is the mass of gridcell i and the global ocean has J gridcells,
 188 and $r_i = 0$ for all $i > J$). By construction, the sum of elements of \mathbf{r} is equal to
 189 one ($\|\mathbf{r}\|_1 \equiv 1$) as is usual in averaging equations. As three-dimensional fields
 190 are modeled for temperature and salinity, the mass of each gridcell is determined

191 by the product of the cell volume and the seawater density as calculated by the
 192 international thermodynamic equation of state (IOC, 2010). Although the LGM
 193 density field is not well constrained, the spatial range of density has variations no
 194 larger than 5%, and thus volume (set by the size of the gridcells) dominates the
 195 calculation.

Substituting the global-mean equation (4) into the definition of the global-mean covariance, the uncertainty of the global mean is clearly dependent upon the uncertainty over the entire globe:

$$\mathbf{C}_{\bar{c}} = \mathbf{r}^T \mathbf{C}_{\tilde{\mathbf{x}}} \mathbf{r}, \quad (5)$$

where $\mathbf{C}_{\tilde{\mathbf{x}}}$ is the full solution covariance. Thus it is necessary to determine the uncertainty of the three-dimensional tracer distribution to calculate the uncertainty of the global mean. Following Appendix B, the solution covariance is

$$\mathbf{C}_{\tilde{\mathbf{x}}} = (\mathbf{S}^{-1} + \mathbf{E}^T \mathbf{W}^{-1} \mathbf{E} + \mathbf{L}_{\tilde{\mathbf{x}}}^T \mathbf{Q}^{-1} \mathbf{L}_{\tilde{\mathbf{x}}})^{-1}, \quad (6)$$

196 where $\mathbf{L}_{\tilde{\mathbf{x}}}$ is the model linearized about the state, $\tilde{\mathbf{x}}$ (i.e., $\mathbf{L}_{\tilde{\mathbf{x}}} \equiv \partial \mathcal{L} / \partial \mathbf{x} |_{\tilde{\mathbf{x}}}$). Equation
 197 (6) assumes that the weight matrices are chosen to be the expected second-
 198 moment matrices of the residuals (i.e., $\mathbf{R}_{mm} = \mathbf{W}$, $\mathbf{R}_{qq} = \mathbf{Q}$, and $\mathbf{R}_{xx} = \mathbf{S}$, follow-
 199 ing Wunsch (1996)), as well as the assumption that our simplified cost function is
 200 valid.

Substitution of equation (6) into (5) permits the global-mean uncertainty to be written explicitly in terms of the known input variables in the problem:

$$\mathbf{C}_{\bar{c}} = \mathbf{r}^T (\mathbf{S}^{-1} + \mathbf{E}^T \mathbf{W}^{-1} \mathbf{E} + \mathbf{L}_{\tilde{\mathbf{x}}}^T \mathbf{Q}^{-1} \mathbf{L}_{\tilde{\mathbf{x}}})^{-1} \mathbf{r}. \quad (7)$$

201 Equation (7) illustrates that the three contributions to the uncertainty come from
 202 the three constraints: the first-guess uncertainty in the state (\mathbf{S}^{-1}), the uncertainty

203 related to the observations ($\mathbf{E}^T \mathbf{W}^{-1} \mathbf{E}$), and the uncertainty related to the imperfect
 204 model ($\mathbf{L}_{\bar{\mathbf{x}}}^T \mathbf{Q}^{-1} \mathbf{L}_{\bar{\mathbf{x}}}$). While these three terms have clear contributions to the uncer-
 205 tainty, they are under the inverse in the equation and thus the total uncertainty is
 206 not simply a linear combination of the three parts.

207 **3. LGM $\delta^{13}\text{C}$ and deglacial change**

208 *3.1. Global-mean $\delta^{13}\text{C}$*

209 The glacial-mean $\delta^{13}\text{C}$ and its uncertainty are calculated by adapting equa-
 210 tions (4) and (7) for $\delta^{13}\text{C}_{\text{DIC}}$. The full solution uncertainty (equation 6) is never
 211 needed explicitly, thus avoiding the storage of a 1.8 terabyte matrix (the state has
 212 475773 elements and $\mathbf{C}_{\bar{\mathbf{x}}}$ has this dimension squared). As \mathbf{r} is a column vector, we
 213 can break equation (7) into two parts, one a matrix-vector product and one a vec-
 214 tor inner product, such that memory usage is minimized. We find that the LGM
 215 mean $\delta^{13}\text{C}_{\text{DIC}}$ is $\overline{\delta^{13}\text{C}_{\text{DIC}}^G} = 0.14\text{‰} \pm 0.20\text{‰}$ (at the 2σ uncertainty level). This
 216 uncertainty estimate accounts for the observational sparsity and measurement er-
 217 ror, but does not include errors incurred by the assumed $\delta^{13}\text{C}$ proxy equation (to
 218 be addressed later in Section 4.6).

219 We are motivated by the atmospheric CO_2 change of 80-100ppm from the
 220 LGM to the pre-industrial era, and thus we seek to estimate the deglacial ma-
 221 rine $\delta^{13}\text{C}$ change, here denoted $\Delta_{\text{MG}}[\delta^{13}\text{C}_{\text{DIC}}]$ (i.e., modern, “M,” minus glacial,
 222 “G”). A modern-day reference circulation that attempts to reconstruct the pre-
 223 industrial ocean was produced using the same method (Gebbie, 2014) and will be
 224 used for comparison here. The GLODAP and CARINA seawater $\delta^{13}\text{C}_{\text{DIC}}$ com-
 225 pilation (Schmittner et al., 2013) constrained the modern-day distribution, and
 226 observations in the upper 1 km of the water column were downweighted to ac-

227 count for the Suess effect (e.g., Olsen et al., 2006) and to produce a pre-industrial
228 gridded $\delta^{13}\text{C}_{\text{DIC}}$ distribution. The result is a reference modern-day estimate of
229 $\overline{\delta^{13}\text{C}_{\text{DIC}}}^M = 0.47\text{‰} \pm 0.03\text{‰}$. Uncertainty due to the Suess effect is not included
230 in this error bar, and is revisited in more detail in Section 4.3 where we find that it
231 may increase the uncertainty by approximately 0.05‰ .

232 Under the assumption that the LGM and modern estimates are independent,
233 the LGM-to-modern difference is $\Delta_{\text{MG}}[\overline{\delta^{13}\text{C}_{\text{DIC}}}] = 0.32\text{‰} \pm 0.20\text{‰}$ (at the 2σ level
234 after rounding). Our estimate provides corroborating evidence for both 1) recent
235 data-based estimates of $0.34\text{‰} \pm 0.26\text{‰}$ (Ciais et al., 2012) and $0.34\text{‰} \pm 0.19\text{‰}$
236 (Peterson et al., 2014), and 2) a forward circulation model that reproduced about
237 100 observations and found a change of $\Delta_{\text{MG}}[\overline{\delta^{13}\text{C}_{\text{DIC}}}] = 0.31\text{‰} \pm 0.20\text{‰}$ (Tagli-
238 abue et al., 2009). Note that the data-based estimates were actually glacial-to-Late
239 Holocene differences (here distinguished by the notation, $\Delta_{\text{HG}}[\delta^{13}\text{C}_{\text{DIC}}]$) that may
240 reflect a different quantity due to the core information ending over the last few
241 thousand years of the Holocene. The level of agreement is surprising, especially
242 considering that our estimate results from a spatially structured pattern of change,
243 shown next.

244 3.2. Spatial distribution of LGM $\delta^{13}\text{C}$

245 The glacial state estimate faithfully reproduces the LGM $\delta^{13}\text{C}$ observations
246 in all ocean basins. When comparing basin-wide zonally averaged $\delta^{13}\text{C}_{\text{DIC}}$ to the
247 foraminiferal observations (squares versus the background colors in Figure 1),
248 the spatial pattern is in broad agreement. Any visual differences are attributable
249 either to an actual misfit of the data or an artifact of zonal variability (i.e., the
250 collapsed third dimension). To eliminate the effect of zonal variability, the state
251 estimate is projected onto the observational locations using a linear interpolation

252 or extrapolation from the 8 nearest gridpoints. The resulting $\delta^{13}\text{C}_{\text{DIC}}$ distribution
253 fits the observations with a standard deviation of the misfit of 0.19‰ that is an
254 acceptable fit within the expected uncertainty of 0.2‰ in the data. 50% of the
255 points are fit within 0.02‰ , although outliers larger than $\pm 0.6\text{‰}$ exist. While not
256 being the primary variable of interest here, $\delta^{18}\text{O}$ is also fit well, with a standard
257 deviation of 0.22‰ that is approximately equal to its expected value of 0.2‰ .

258 The main characteristic of the LGM Atlantic $\delta^{13}\text{C}$ distribution is a depletion
259 of $\delta^{13}\text{C}_{\text{DIC}}$ below 2500 meters depth (upper panel, Figure 1) that conforms with
260 expectations (e.g., Duplessy et al., 1988; Curry and Oppo, 2005). The North At-
261 lantic is characterized by a mixing zone from 2 to 4 km depth with a nearly con-
262 stant vertical gradient from 0.8‰ to 0‰ . The zonally-averaged South Atlantic,
263 however, does not have a gradient as sharp as seen in the Brazil Margin data or
264 the map of Curry and Oppo (2005), but can be explained by observations of lower
265 $\delta^{13}\text{C}$ values in the eastern South Atlantic between 2 and 3 km depth. Of more
266 concern are the undersampled regions, where this inversion sometimes disagrees
267 with the Gebbie (2014) inversion. For example, the updated state estimate has a
268 much higher $\delta^{13}\text{C}_{\text{DIC}}$ in the Arctic (1.2‰ compared to 0.6‰). The most depleted
269 values in the Southern Ocean are about -0.8‰ in both inversions, but should not
270 necessarily be interpreted as a robust result. The uncertainty of the estimate in
271 these regions without data will be explicitly addressed in the next section.

272 The state estimate permits the inference of more $\delta^{13}\text{C}_{\text{DIC}}$ structure in the Pa-
273 cific and Indian Oceans (middle and lower panels, Figure 1) than was previously
274 mapped, due in large part to the larger data compilation and the smoothing ca-
275 pabilities of the model used here. The zonally-averaged Pacific picture masks
276 significant zonal variability, including a deepening of the most depleted western

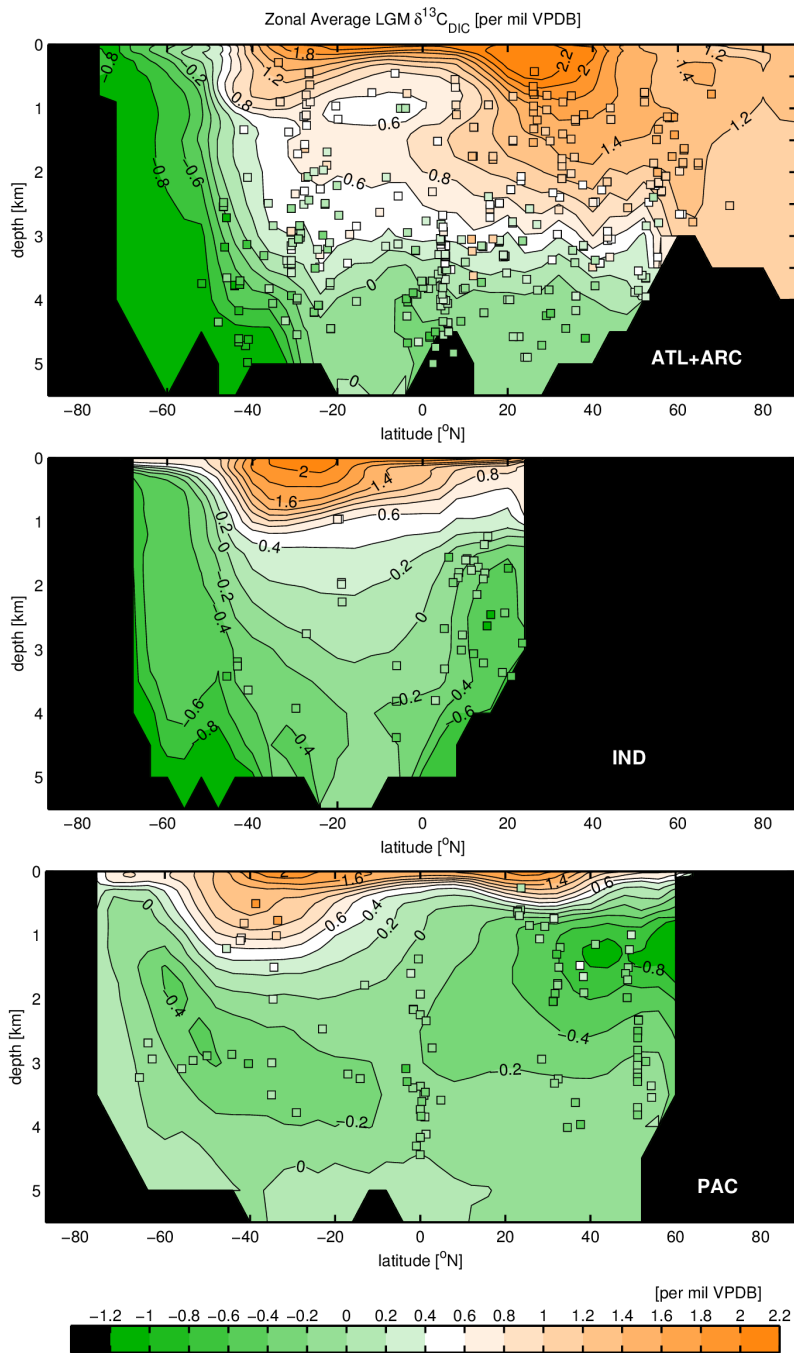


Figure 1: Zonally-averaged, LGM $\delta^{13}\text{C}_{\text{DIC}}$ divided into three sections: the Atlantic and Arctic (*upper*), Indian (*middle*), and Pacific (*lower*), with all observations from the particular basin (*colored squares*) and 3D gridded field (*background colors and contours*). The oceans are divided according to Figure 7 of Gebbie and Huybers (2010). The colored symbols are on the same color scale as the background field.

277 Pacific $\delta^{13}\text{C}_{\text{DIC}}$ from 1.5 km in the modern-day to almost 3 km during the LGM
278 (e.g., Matsumoto et al., 2002; Herguera et al., 2010). There are significant differ-
279 ences with previous maps, however, including a closed region of depleted $\delta^{13}\text{C}_{\text{DIC}}$
280 due to remineralization north of 40°N in the North Pacific not seen by Herguera
281 et al. (2010). The Indian Ocean is reconstructed as a hybrid of the other oceans,
282 with low- $\delta^{13}\text{C}_{\text{DIC}}$ Southern Ocean bottom waters like the Atlantic, but a lack of
283 high- $\delta^{13}\text{C}_{\text{DIC}}$ waters at mid-depths like the Pacific.

284 The bottom waters of the Southern Ocean have $\delta^{13}\text{C}_{\text{DIC}}$ differences approach-
285 ing 1‰ between the Ross (0‰) and Weddell (-0.8‰) Seas that are masked by
286 the zonal averages. These horizontal gradients are partially explained as the pro-
287 jection of the large vertical $\delta^{13}\text{C}_{\text{DIC}}$ gradients into the horizontal by the patchiness
288 of northern source water incursion into the Southern Ocean. The inhomogeneities
289 do not appear to reflect any major shift in the transport of the Antarctic Circumpo-
290 lar Current, as northern-source waters continue to spread eastward into the Indian
291 Ocean over a similar range as the modern day. While major circulation changes
292 are not implicated, the model reconstructs a greater filling of the abyss by the
293 Ross Sea rather than the Weddell Sea. Increased glacial abyssal mixing and a
294 vigorous deep circulation could explain this feature (Wunsch, 2003; Arbic et al.,
295 2004; Schmittner et al., 2015), but our current model lacks absolute rate informa-
296 tion and cannot directly test this hypothesis.

297 Besides the $\delta^{13}\text{C}$ distribution, the state estimate permits the diagnosis of water-
298 mass distributions consistent with the seawater properties. The inferred LGM At-
299 lantic water-mass geometry is similar to the previous inversion of Gebbie (2014),
300 where southern source waters dominate the ocean composition only below 4 km
301 depth in the North Atlantic. In other words, the southern source waters contribute

302 50% or more of the water by mass in that limited region. Significant deep rem-
303 ineralization (with the addition of ^{12}C effectively causing a sink of $\delta^{13}\text{C}$) was
304 originally reported in the deep glacial Atlantic (Gebbie, 2014), but is less pro-
305 nounced in the updated state estimate due to the use of a more spatially-coherent
306 $\delta^{18}\text{O}$ dataset (derived from LGM-to-Late Holocene differences). The estimated
307 LGM Pacific has deeper North Pacific Water (down to 2 km instead of 800 m to-
308 day, as defined by the 50% concentration line). Otherwise southern water masses
309 fill the same part of the Pacific sector.

310 *3.3. Spatial pattern of $\delta^{13}\text{C}$ change*

311 The difference of the modern-day and LGM $\delta^{13}\text{C}_{\text{DIC}}$ permits the mapping of
312 a global, three dimensional field of $\Delta_{\text{MG}}[\delta^{13}\text{C}_{\text{DIC}}]$, where large-scale coherent pat-
313 terns emerge (Figure 2). In much of the world ocean above 1 km depth, $\delta^{13}\text{C}_{\text{DIC}}$
314 decreased over the deglaciation despite the increase in the global mean. Even the
315 North Pacific, which was previously found to have little $\delta^{13}\text{C}_{\text{DIC}}$ change above 2
316 km (Matsumoto et al., 2002), is estimated to contain upper ocean regions with
317 deglacial $\delta^{13}\text{C}$ decreases. In general, $\Delta_{\text{MG}}[\delta^{13}\text{C}_{\text{DIC}}]$ increases with depth and to-
318 ward the south, with the biggest changes reserved for the Atlantic sector of the
319 Southern Ocean. From these maps, it is clear that the competing influence of many
320 different regions must be included in order to accurately assess the the global
321 mean.

322 **4. Contributions to uncertainty**

323 *4.1. Observational sensitivity*

324 Obvious candidates to contribute to the uncertainty include the sparsity, mea-
325 surement error, and representativeness of the observations. Here we test how the

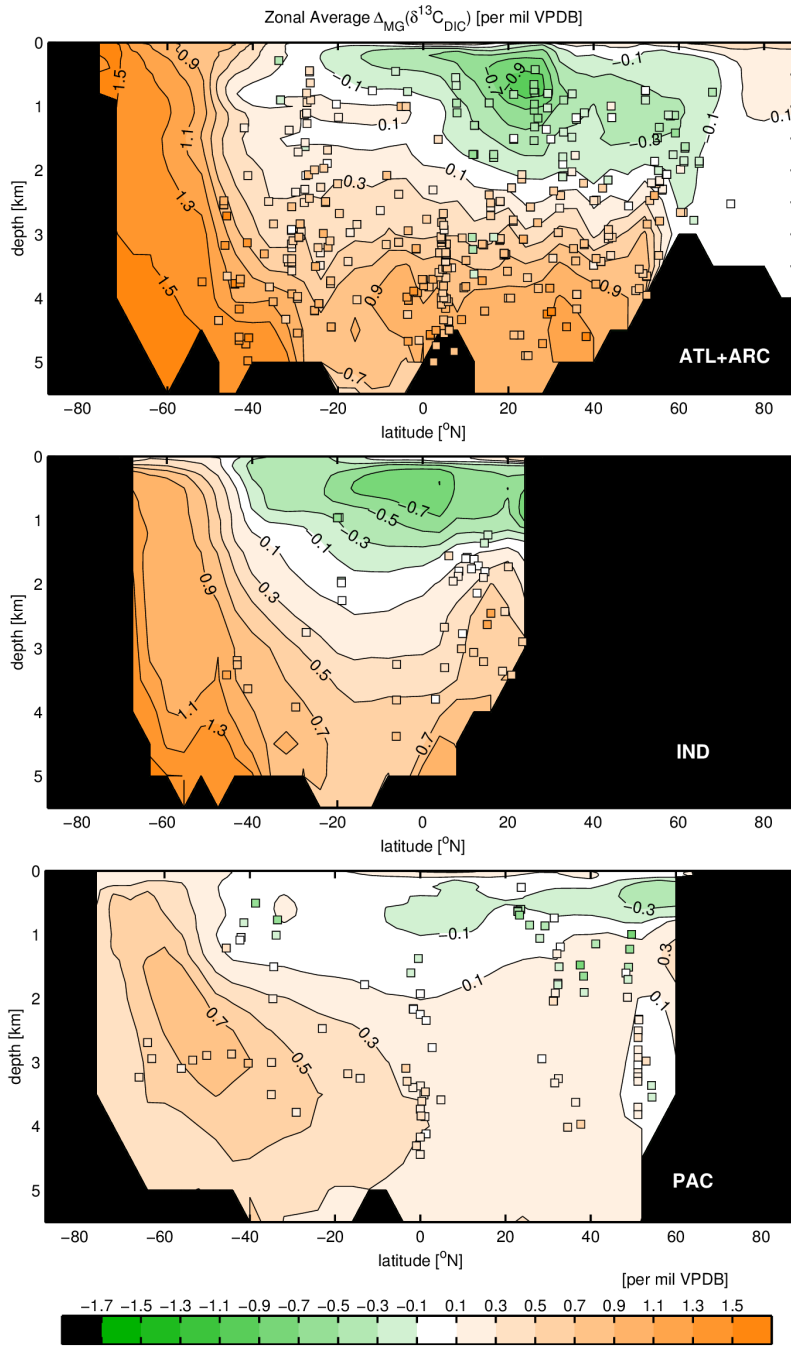


Figure 2: Similar to Figure 1, but for the Atlantic, Indian, and Pacific zonal-average difference in $\delta^{13}C_{DIC}$ between the modern-day and LGM (i.e., $\Delta_{MG}[\delta^{13}C_{DIC}] = \delta^{13}C_{DIC}^M - \delta^{13}C_{DIC}^G$).

326 number of sediment core observations affects the resulting uncertainty by creating
 327 hypothetical cases with a range of observations from 10 to 15000. For the cases
 328 where the number of observations is less than observed in reality, we randomly
 329 select a subset of the true observations. This constraint is symbolically written:
 330 $\check{\mathbf{y}} = \check{\mathbf{E}}\mathbf{x} + \check{\mathbf{n}}$, where the variables with the breve mark have rows deleted from the
 331 original \mathbf{E} definition (second term on the right hand side of equation 7). The
 332 actual observational values do not matter in this calculation, but only that the ob-
 333 servational term is modified. For hypothetical cases with more observations than
 334 reality, we augment the actual observations with additional observations taken ran-
 335 domly from the seafloor, although this is not entirely realistic due to issues with
 336 carbonate preservation, species habitats, and sediment availability. Five trials are
 337 performed with the modified $\check{\mathbf{E}}$ matrix and the mean of the trials is reported to
 338 help make the results more robust.

339 The uncertainty decreases with an increasing number of observations accord-
 340 ing to an apparent power law ($\sigma_{\bar{c}} \approx 2\%_0/\sqrt{N}$), where N is the number of ob-
 341 servations (Figure 3). This function is consistent with the uncertainty estimate
 342 for the actual number of observations ($2\sigma_{\bar{c}} = 0.20\%_0$ for $N = 492$). Between
 343 $N = 500$ and $N = 1000$, the slope of the power law increases, suggesting that
 344 the additional randomly-distributed data points potentially sample the ocean more
 345 efficiently than the irregularly-clustered 492 data points that are actually avail-
 346 able, and indicating that a strategic sampling plan (e.g., see Section 4.5) could
 347 produce an even greater reduction in uncertainty. Limitations on the presence of
 348 *Cibicidoides* calcite on the seafloor would also provide a constraint for a sampling
 349 strategy. In tests where the number of observations is increased past 15000, the
 350 standard error does not decrease below $0.06\%_0$, suggesting that seafloor observa-

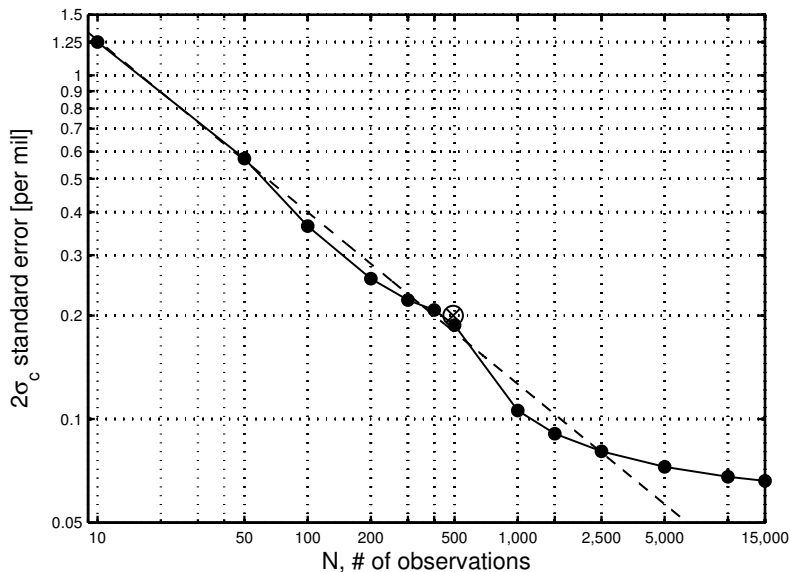


Figure 3: The $2\sigma_{\bar{c}}$ standard error of the glacial-mean $\delta^{13}\text{C}_{\text{DIC}}$ as a function of number of observations, on a log-log set of axes. Each dot represents the average of five trials. For $N = 10$ to $N = 400$, a subset of actual observational locations is used. For $N = 500$ to 15000, the 492 actual observations are augmented with observations randomly distributed along the lateral and bottom oceanic boundaries. A power law (*dashed line*) approximately fits the function: $\sigma_{\bar{c}} \approx 2\%_0/\sqrt{N}$ where N is the number of observations. The LGM state estimate is also plotted (*circle with an X*).

351 tions are eventually limited in their ability to record interior ocean signals due to
 352 their location and the remaining measurement error. In summary, we expect that
 353 the uncertainty on global-mean $\delta^{13}\text{C}_{\text{DIC}}$ would be halved with a fourfold increase
 354 in the number of observations.

355 4.2. Circulation dependence

356 A second major contributor to uncertainty is the circulation field because
 357 knowledge of the flow paths permits extrapolation over the large distances be-
 358 tween paleo-data. In our steady-state scenario, the mass fluxes are expressed as

359 dimensionless mass flux ratios, \mathbf{m} , that are bounded by 0 and 1 (recall the discus-
360 sion of the model in Section 2.1). Here we calculate how the global-mean standard
361 error depends upon the assumed uncertainty in the circulation. All input variables
362 are kept constant in equation (7) except the part of the \mathbf{S}^{-1} matrix correspond-
363 ing to the circulation is adjusted. For hypothetical cases where the circulation is
364 known as well or better than the modern-day ($\sigma_m < 0.05$), the resulting global
365 mean uncertainty is small (0.03‰), but it cannot be further reduced due to the ob-
366 servational characteristics (Figure 4). This limit is lower than previously estimated
367 (e.g., 0.26‰, Ciais et al., 2012), and might result from the improved reconstruc-
368 tion ability of the state estimate. For circulation uncertainties greater than 0.05,
369 the standard error increases from 0.05‰ to 0.6‰ with increasing circulation un-
370 certainty, and follows an approximate exponential relation (i.e., $\sigma_c \approx 0.6‰ \sigma_m^{0.9}$).
371 The prior estimate of circulation uncertainty, σ_m , is a difficult quantity to estimate,
372 and here we have suggested that a reasonable value is 0.3. The reported error of
373 global-mean $\delta^{13}\text{C}_{\text{DIC}}$ is sensitive to this choice, however, as is shown in Figure 4.
374 The sensitive dependence originates from the use of the circulation to interpolate
375 and extrapolate over the data-void regions of the globe.

376 4.3. Regional analysis

377 A more traditional means of analysis is to break the ocean into subdomains to
378 quantify the geographic contributions to global-mean uncertainty. Here, regional
379 means are calculated by taking subdomains of the global domain and recalculating
380 the mass-weighting vector, \mathbf{r} , in equation (7). Specifically, the elements of \mathbf{r} that
381 correspond to locations outside the region of interest are set to zero, and the vector
382 is renormalized such that the elements sum to one. Here we select 13 regions of
383 interest in order to compare to the recent work of Peterson et al. (2014).

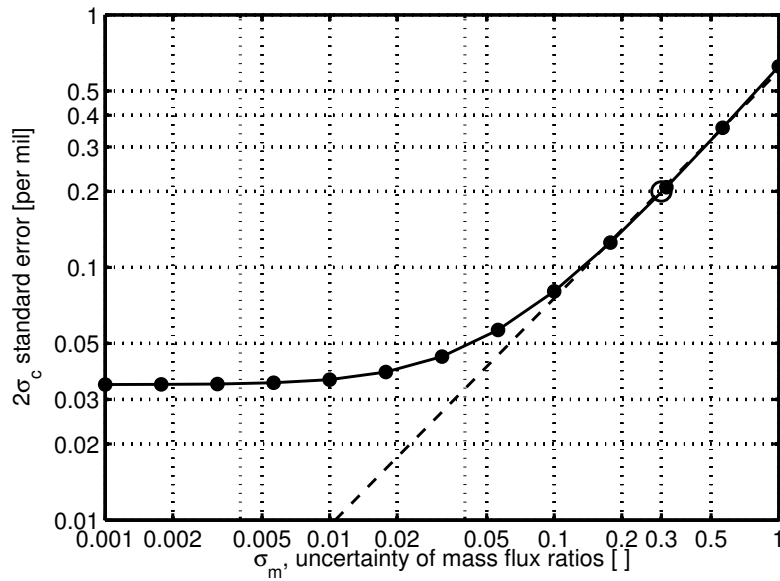


Figure 4: Similar to Figure 3, but the standard error ($2\sigma_{\bar{c}}$) of the glacial-mean $\delta^{13}\text{C}_{\text{DIC}}$ as a function of how well the circulation is known (in terms of the uncertainty of nondimensional mass-flux ratios, σ_m). An uncertainty of $\sigma_m = 1$ in the mass-flux ratios represents zero circulation knowledge. The glacial circulation uncertainty is chosen to be 0.3 (*circle*). The function roughly asymptotes to the function, $\sigma_{\bar{c}} \approx 0.3\text{‰} \sigma_m^{0.9}$ (*dashed line*).

Region	$\Delta_{\text{MG}}[\overline{\delta^{13}\text{C}_{\text{DIC}}}]$	$\overline{\delta^{13}\text{C}_{\text{DIC}}}^M$	N_M	μ_M	σ_M	$\overline{\delta^{13}\text{C}_{\text{DIC}}}^G$	N_G	μ_G	σ_G
Global	0.32 ± 0.20	0.47 ± 0.03	19922	0.09	0.27	0.14 ± 0.20	492	0.01	0.19
Deep	0.49 ± 0.23	0.37 ± 0.02	229	0.05	0.21	-0.12 ± 0.22	0	-	-
Surface	0.07 ± 0.71	1.06 ± 0.07	8453	0.21	0.36	1.01 ± 0.70	6	-0.01	0.05
NW Atlantic	0.16 ± 0.67	0.96 ± 0.06	321	0.11	0.20	0.80 ± 0.67	72	-0.02	0.18
NE Atlantic	0.25 ± 0.85	0.99 ± 0.25	540	0.10	0.15	0.74 ± 0.81	155	0.01	0.22
SW Atlantic	0.41 ± 0.31	0.77 ± 0.02	836	-0.03	0.14	0.36 ± 0.31	45	0.06	0.23
SE Atlantic	0.60 ± 0.21	0.72 ± 0.05	274	0.00	0.13	0.12 ± 0.20	79	0.04	0.23
South Atlantic	0.84 ± 0.40	0.62 ± 0.06	23	0.21	0.20	-0.22 ± 0.40	23	0.02	0.27
North Pacific	0.13 ± 0.27	-0.08 ± 0.02	1254	0.03	0.22	-0.21 ± 0.27	65	-0.01	0.11
South Pacific	0.33 ± 0.33	0.35 ± 0.01	4157	0.00	0.15	0.02 ± 0.33	36	0.00	0.08
Indian	0.25 ± 0.32	0.34 ± 0.01	2735	-0.04	0.12	0.09 ± 0.32	42	0.02	0.12
Southern (AI)	1.22 ± 0.85	0.54 ± 0.03	648	0.06	0.10	-0.68 ± 0.85	0	-	-
Southern (P)	0.44 ± 0.30	0.45 ± 0.02	401	0.01	0.10	0.01 ± 0.30	1	0.07	-

Table 1: Mean $\delta^{13}\text{C}_{\text{DIC}}$ with error estimates and statistics for 13 oceanic regions defined by Peterson et al. (2014). The quantities include (*from left column to right*): global-mean LGM-to-modern $\delta^{13}\text{C}$ change and 2σ uncertainty ($\Delta_{\text{MG}}[\overline{\delta^{13}\text{C}_{\text{DIC}}}]$), modern-day mean $\delta^{13}\text{C}_{\text{DIC}}$ and 2σ uncertainty ($\overline{\delta^{13}\text{C}_{\text{DIC}}}^M$), number of modern-day observations (N_M), mean modern-day model-data misfit (μ_M), standard deviation of modern-day model-data misfit (σ_M), LGM mean $\delta^{13}\text{C}_{\text{DIC}}$ and 2σ uncertainty ($\overline{\delta^{13}\text{C}_{\text{DIC}}}^G$), number of LGM observations (N_G), mean LGM model-data misfit (μ_G), and standard deviation of LGM model-data misfit (σ_G). Three large-scale regions are included: Global, Deep (everywhere below 5 km depth), and Surface (everywhere shallower than 500 m). The Atlantic is split into five regions: NW (west of 33°W , north of 0°), NE (east of 33°W , north of 0°), SW (west of 15°W , 0° to 55°S), SE (east of 15°W , 0° to 55°S), and South Atlantic (east of 22°W , 40°S to 55°S). The Pacific is split into two regions: North Pacific (0° to 60°N) and South Pacific (0° to 66°S). The Indian Ocean is defined as one region (north of 55°S , 30°E to 125°E). The Southern Ocean is split into two parts: Atlantic-Indian (AI) sector (south of 55°S) and the Pacific (P) sector (south of 66°S). See Figure 1 of Peterson et al. (2014) for complete boundaries.

384 The primary geographic contributors to global-mean uncertainty are the Sur-
385 face and North Atlantic regions ($2\sigma_{\bar{c}} > 0.6\text{‰}$ in Table 1). This result does not
386 straightforwardly proceed from a consideration of the number of observations in
387 any given region. For example, both the Surface and Deep regions have less than
388 10 observations, yet the Deep region has much more moderate uncertainty (0.23‰
389 versus 0.70‰ in the Surface). Waters that enter the Deep region must pass through
390 observations at shallower depths, and are therefore somewhat constrained by the
391 tracer transport model and observations. The uncertainty in the North Atlantic
392 occurs despite over 200 LGM observations in those regions, and results from the
393 nearly-unobserved $\delta^{13}\text{C}_{\text{DIC}}$ values in the Nordic, Mediterranean, and Caribbean
394 Seas. The center of the North Atlantic, on the other hand, has some of the lowest
395 estimated errors, but this is masked by our choice of regional boundaries.

396 Up to this point, we have emphasized the agreement of our global-mean esti-
397 mate with previous studies, and generally speaking, our regional results are also
398 consistent with previous regional estimates (e.g., Oliver et al., 2010; Peterson
399 et al., 2014). In a detailed investigation of the Deep ($> 5\text{km}$) region, however,
400 our model reconstructs a 0.49‰ change, suggesting that the 0.74‰ estimate of
401 Peterson et al. (2014) is an overestimate owing to the extrapolation by their as-
402 sumed linearly-varying vertical structure. In the Surface region, there are similar-
403 ities between the estimates (here: $\Delta_{\text{MG}}[\overline{\delta^{13}\text{C}_{\text{DIC}}}] = 0.07\text{‰} \pm 0.71\text{‰}$, Peterson et al.
404 (2014): $\Delta_{\text{HG}}[\overline{\delta^{13}\text{C}_{\text{DIC}}}] = 0.02\text{‰} \pm 0.40\text{‰}$), but our more sophisticated reconstruc-
405 tion technique yields larger uncertainty, suggesting that their ad-hoc error bar is
406 an underestimate.

407 Our large Surface region error bars indicate that the best place to isolate a
408 reservoir from benthic foraminiferal detection is not the bottom ocean, but instead

409 the upper thermocline waters that primarily recirculate in the subtropics and trop-
410 ics. This result points to the need to compile planktonic $\delta^{13}\text{C}_{\text{DIC}}$ records (e.g.,
411 Broecker and McGee, 2013) so that they can be used in concert with benthic
412 records. In this regard we note that there is convincing evidence indicating the
413 $\delta^{13}\text{C}$ of planktonic foraminifera shells vary with seawater carbonate ion concen-
414 tration (Spero et al., 1997; Russell and Spero, 2000; Peeters et al., 2002). Al-
415 though this effect has not been identified in benthic foraminifera, its pervasive
416 presence among many species of planktonic foraminifera suggests that deep wa-
417 ter carbonate ion variations between the modern and glacial could shift benthic
418 foraminifera shell $\delta^{13}\text{C}$ away from a 1:1 relationship with $\delta^{13}\text{C}_{\text{DIC}}$ and contribute
419 to uncertainties in these modeled reconstructions (see Section 4.6).

420 4.4. $\delta^{13}\text{C}$ Suess effect

421 The model fits the observations to an acceptable level in almost all regions, as
422 evidenced by the standard deviation of the modern and glacial model-data misfits,
423 σ_M and σ_G , being less than or equal to 0.2‰. One exception is the modern-day
424 surface ($\sigma_M = 0.36‰$) which may be symptomatic of seasonal variations not cap-
425 tured by the steady-state model. The model-data misfit also has a strong mean
426 offset in the modern-day surface ocean ($\mu_M = 0.21‰$), where the state estimate
427 has more positive $\delta^{13}\text{C}_{\text{DIC}}$ values than the GLODAP/CARINA observations. This
428 upper ocean effect has consequences for the global statistics, as the modern-day
429 state estimate is on average 0.09‰ more enriched in $\delta^{13}\text{C}_{\text{DIC}}$ than the observa-
430 tions over the entire world ocean. The sign of the misfit is consistent with the
431 observations being contaminated by anthropogenically-derived $\delta^{13}\text{C}_{\text{DIC}}$.

432 Although the state estimation methodology appears able to filter the Suess
433 effect by downweighting $\delta^{13}\text{C}_{\text{DIC}}$ datapoints in the upper ocean (i.e., expecting

434 larger errors for these points, recall Section 3.1), we still need to consider whether
 435 the implied magnitude of the effect is plausible. To quantify the effect of this
 436 downweighting, we additionally invert a case that represents the 1990s where all
 437 modern-day $\delta^{13}\text{C}_{\text{DIC}}$ observations are weighted equally. The data is still well-fit
 438 for the 1990s case ($\sigma_M = 0.11\text{‰}$), but the mean $\delta^{13}\text{C}_{\text{DIC}}$ is shifted to $\overline{\delta^{13}\text{C}_{\text{DIC}}}^M =$
 439 0.41‰ : 0.06‰ less than our original modern-day (pre-industrial) estimate. The
 440 spatial pattern of the difference (Figure 5) shows similarities to the expected Suess
 441 effect, such as enhanced uptake and negative values in the North Atlantic deep
 442 water formation sites and the subtropical gyres. Features in the deep Pacific are
 443 unlikely to be the Suess effect, but more likely reflect changes in how the data
 444 is extrapolated into data-sparse regions. The estimated LGM-to-modern $\delta^{13}\text{C}_{\text{DIC}}$
 445 change directly depends upon the handling of the Suess effect, and here the ac-
 446 counting for the contaminated $\delta^{13}\text{C}_{\text{DIC}}$ values (by downweighting) leads to an
 447 $\Delta_{\text{MG}}[\overline{\delta^{13}\text{C}_{\text{DIC}}}]$ value that is 0.06‰ higher than would otherwise have been esti-
 448 mated.

449 To check whether the magnitude of our Suess effect correction is reason-
 450 able, another inversion is produced where the anthropogenic $\delta^{13}\text{C}_{\text{DIC}}$ signal is re-
 451 moved from seawater measurements using the “FeL” simulation of Schmittner
 452 et al. (2013). To do so, we first project the modeled estimate of 1990s anthro-
 453 pogenic $\delta^{13}\text{C}_{\text{DIC}}$ onto the data locations and subtract it from the observations to
 454 make a corrected dataset. Then the state estimate is re-derived by weighting
 455 all data equally. By this method, the mean pre-industrial $\delta^{13}\text{C}_{\text{DIC}}$ is $\overline{\delta^{13}\text{C}_{\text{DIC}}}^M =$
 456 0.49‰ , not significantly different than our original estimate of $\overline{\delta^{13}\text{C}_{\text{DIC}}}^M = 0.47\text{‰} \pm$
 457 0.03‰ . Thus, state estimation methods suggest that the mean Suess effect is
 458 0.06‰ (from the previous paragraph) or 0.08‰ (this paragraph), both somewhat

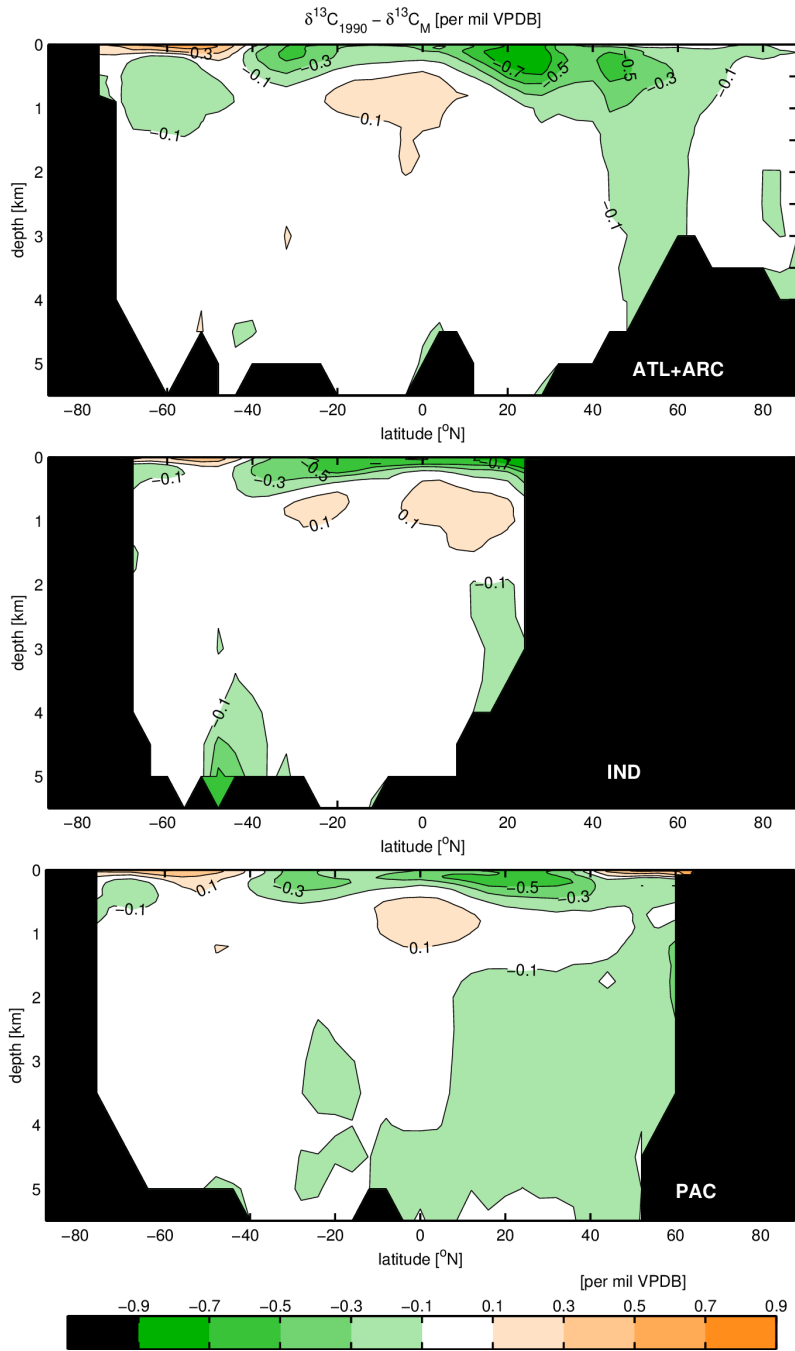


Figure 5: Similar to Figure 2, but for the Atlantic, Indian, and Pacific zonal-average difference between $\delta^{13}\text{C}_{\text{DIC}}$ in the 1990s and the modern (i.e., pre-industrial) case.

459 smaller than a forward model (Tagliabue and Bopp, 2008) that found 0.12‰ when
460 constrained by the observations of Gruber et al. (1999). While we believe that our
461 state estimation methodology has done a reasonable job in assessing the anthro-
462 pogenic signal, an uncertainty of perhaps $\pm 0.05\%$ (loosely based on the spread
463 of the three estimates) still remains in the magnitude of the $\delta^{13}\text{C}$ Suess effect
464 and therefore should be added to the uncertainty of the LGM-to-modern $\delta^{13}\text{C}_{\text{DIC}}$
465 change.

466 4.5. Large $\delta^{13}\text{C}$ change scenario

467 In this section, we seek to confirm that the estimated error bars are plausi-
468 ble, and to visualize where the estimate glacial $\delta^{13}\text{C}_{\text{DIC}}$ field is least constrained.
469 These issues can be addressed in greater detail by performing a test to determine
470 whether a large $\Delta_{\text{MG}}[\overline{\delta^{13}\text{C}_{\text{DIC}}}]$ is consistent with the observations and a steady-
471 state circulation. To perform this test, we add an additional “observation” that the
472 LGM-to-modern $\delta^{13}\text{C}_{\text{DIC}}$ change is just above the upper limit as given by the 2σ
473 error bar: 0.6‰. As in Section 4.1, this modification is handled by introducing a
474 modified observational matrix, vector, and weighting: $\check{\mathbf{E}}$, $\check{\mathbf{y}}$, and $\check{\mathbf{W}}$, that enforces
475 the additional constraint with a small error: $\Delta_{\text{MG}}[\overline{\delta^{13}\text{C}_{\text{DIC}}}] = 0.6\% \pm 0.01\%$. The
476 nonlinear solution method of Section 2.3 is then run with these additions and no
477 other changes.

478 A second LGM state estimate (hereafter, LGM State Estimate 2) is indeed ca-
479 pable of fitting the data while producing a whole-ocean change of $\Delta_{\text{MG}}[\overline{\delta^{13}\text{C}_{\text{DIC}}}] =$
480 0.59‰ (Figure 6). The spatial pattern of remaining model-data misfits do not
481 suggest that the phytodetritus or carbonate ion effect are at play. The implied
482 circulation leads to a deep (greater than 3 km) northern-southern water-mass in-
483 terface in the Atlantic Ocean, similar to that in LGM estimate 1. The standard

484 deviation of the model-data misfit is actually smaller than that for LGM estimate
485 1 (LGM 1: $\sigma_G = 0.19\%$, LGM 2: $\sigma_{G2} = 0.17\%$). The model-data misfit statistics
486 of LGM state estimate 2 are consistent with what is expected from a 2σ outlier of
487 LGM state estimate 1; the estimated mean model-data misfit of $\mu_{G2} = -0.03\%$ is
488 insignificant at the 5% level, but just so ($p = 0.06$ for $N = 492$). The larger whole-
489 ocean change is due to increased changes in specific regions, such as the Atlantic
490 sector of the Southern Ocean where $\Delta_{MG}[\delta^{13}C_{DIC}] > 1.4\%$. In addition, the uncon-
491 strained Arctic Ocean and Mediterranean Sea have much increased $\Delta_{MG}[\delta^{13}C_{DIC}]$
492 at intermediate levels.

493 The difference in $\delta^{13}C_{DIC}$ between the two LGM state estimates, $\Delta_{GG}[\delta^{13}C_{DIC}]$
494 (the difference of two glacial “G” estimates), can be thought of as the observa-
495 tional null space and illustrates the ocean regions that are both unconstrained and
496 important for setting the global mean. The biggest differences occur at the Pacific
497 surface and the South Indian Ocean (Figure 7). Surface differences, especially
498 in the Pacific Ocean, are as large as 1% , and are consistent with the large error
499 bars previously detailed in Table 1. Should the planktonic $\delta^{13}C$ records that indi-
500 cate little change between the LGM and modern-day (e.g., Broecker and McGee,
501 2013) be representative of the entire tropics, LGM state estimate 1 (from Sections
502 3-5) would be considered more reasonable. Our map of the difference between the
503 two LGM state estimates emphasizes the regions in which additional observations
504 would be most useful.

505 LGM State Estimate 2 may be relevant to more than just checking the ma-
506 chinery for producing error bars, as there are a number of reasons to suspect that
507 the LGM-to-modern $\delta^{13}C_{DIC}$ change might be larger than the recent marine-based
508 consensus. For example, the state estimate reverts to modern-day conditions in

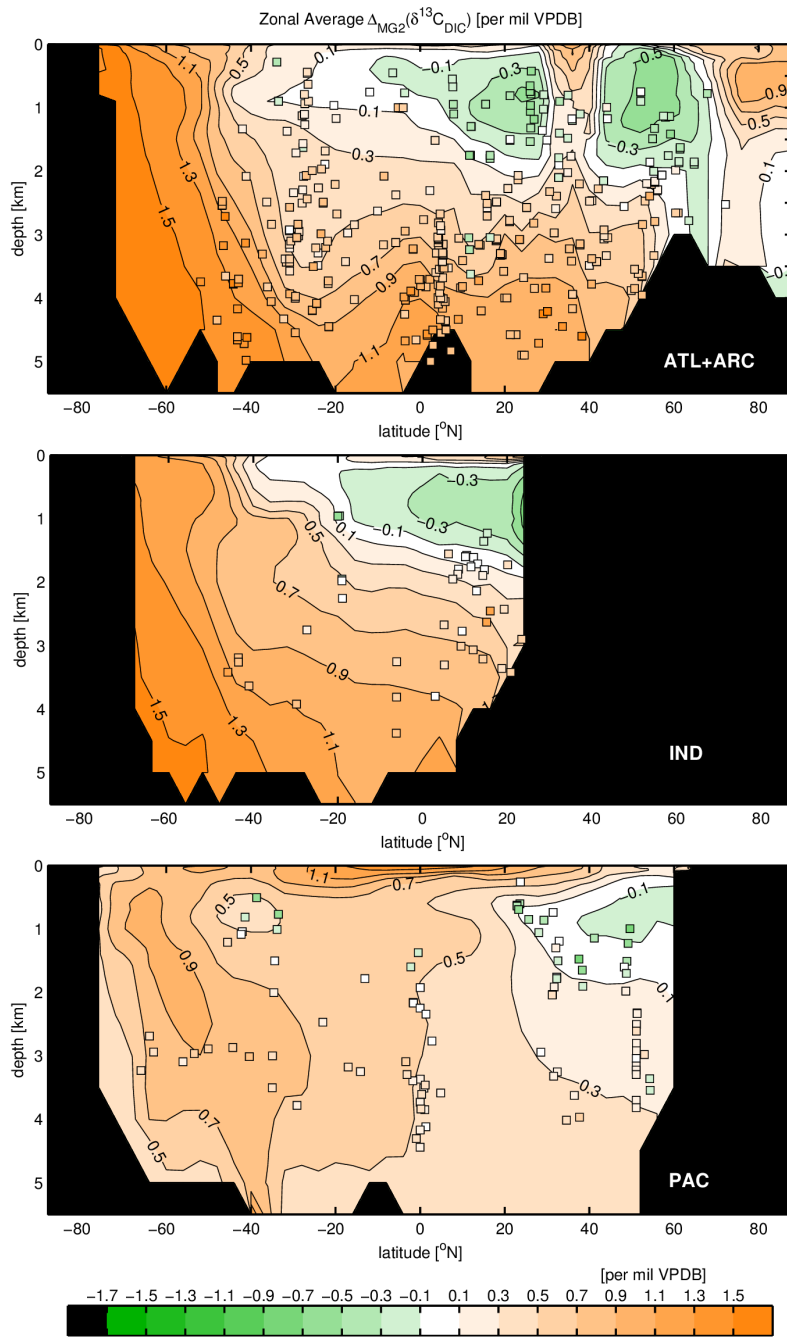


Figure 6: Atlantic (and Arctic), Indian, and Pacific zonal-average difference of $\delta^{13}C$ between LGM State Estimate 2 and modern-day (i.e., $\Delta_{MG}[\delta^{13}C_{DIC}] = \delta^{13}C_{DIC}^M - \delta^{13}C_{DIC}^{G2}$).

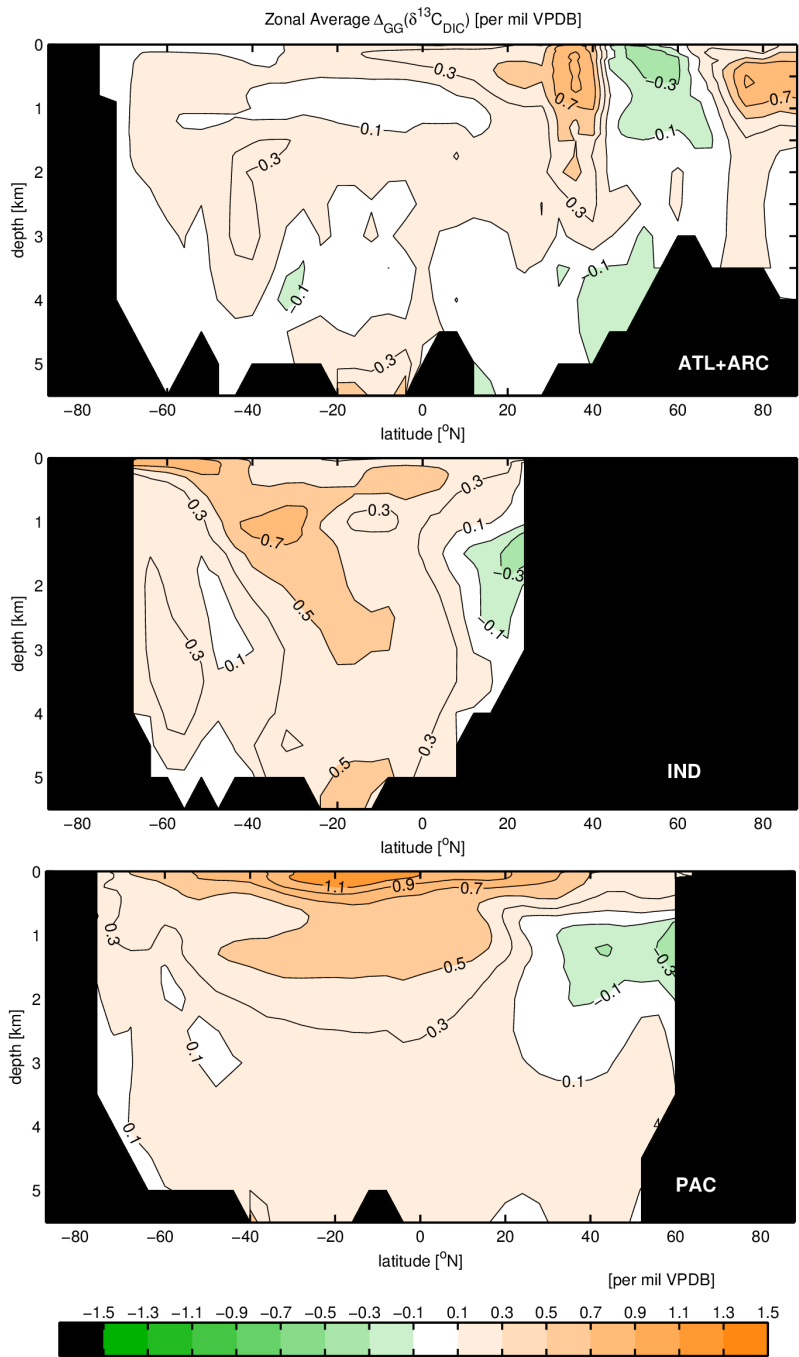


Figure 7: Atlantic and Pacific zonal-average difference of $\delta^{13}C_{DIC}$ between 2 LGM Estimates ($\Delta_{GG}[\delta^{13}C_{DIC}] = \delta^{13}C_{DIC}^G - \delta^{13}C_{DIC}^2$).

509 the absence of any paleo-data and thus, the $\Delta_{\text{MG}}[\overline{\delta^{13}\text{C}_{\text{DIC}}}]$ value from LGM State
510 Estimate 1 could be biased low due to remnant modern-day constraints pulling the
511 estimate toward no change. A low estimate may also be due to low temporal res-
512 olution in the cores, as high-resolution cores can have higher $\Delta_{\text{MG}}[\delta^{13}\text{C}_{\text{DIC}}]$ values
513 (A. Mix, personal communication, 2014). Furthermore, if a $\Delta_{\text{MG}}[\overline{\delta^{13}\text{C}_{\text{DIC}}}]$ value
514 of 0.6‰ is possible, then terrestrial-based (e.g., Crowley, 1995) and marine-based
515 (e.g., Tagliabue et al., 2009) carbon partitioning estimates could be brought into
516 consistency without the need to invoke an inert terrestrial carbon pool (Ciais et al.,
517 2012).

518 4.6. Seawater-to-calcite relationship

519 Here we revisit our definition of $\Delta_{\text{MG}}[\delta^{13}\text{C}_{\text{DIC}}]$ and whether it significantly dif-
520 fers from $\Delta_{\text{HG}}[\delta^{13}\text{C}_{\text{DIC}}]$, defined as the LGM-to-Late Holocene difference. Infor-
521 mation regarding $\Delta_{\text{HG}}[\delta^{13}\text{C}_{\text{DIC}}]$ is more directly available through the difference of
522 LGM and Late Holocene core data, as interlaboratory offsets are canceled by the
523 differencing. One tradeoff is that only 365 measurements of a Late Holocene and
524 LGM value from the same core are available even when the Late Holocene time
525 interval is extended from 0-6 kyr BP. Using the modern-day circulation to recre-
526 ate a global $\delta^{13}\text{C}_{\text{DIC}}$ field using the Late Holocene coretop values, we estimate a
527 Late-Holocene mean value of $\overline{\delta^{13}\text{C}_{\text{DIC}}^H} = 0.55\text{‰} \pm 0.20\text{‰}$ that is 0.08‰ higher
528 than the modern-day estimate. The difference directly affects the inferred LGM-
529 to-modern change and is attributable to Holocene temporal variability (e.g., Oppo
530 et al., 2003) and error in the seawater-to-calcite calibration, but it is difficult to
531 separate the two. In particular, a systematic offset in the $\delta^{13}\text{C}$ calcite-to-seawater
532 proxy relationship could occur due to a dependence of calcite $\delta^{13}\text{C}$ on carbonate
533 ion or temperature (e.g., Spero et al., 1997; Hesse et al., 2014). To determine the

534 size of such an effect, an improved calibration between the Late Holocene $\delta^{13}\text{C}$
 535 values and the modern-day seawater characteristics including $\delta^{13}\text{C}_{\text{DIC}}$, tempera-
 536 ture, salinity, CO_3^{2-} , DIC, and pH should be pursued.

537 **5. Discussion**

538 The discussion aims to put the results of this work into the context of previous
 539 observational methods to estimate LGM-to-modern $\delta^{13}\text{C}_{\text{DIC}}$ change.

540 *5.1. Optimal data weights*

Given a circulation field, the state estimate formulation permits the coefficients and constants of equation (1) to be explicitly calculated. Following Appendix C, the optimal set of data weights is

$$\mathbf{w} = \mathbf{W}^{-1}\hat{\mathbf{E}}(\hat{\mathbf{S}}^{-1} + \hat{\mathbf{E}}^T\mathbf{W}^{-1}\hat{\mathbf{E}} + \mathbf{L}_c^T\mathbf{Q}^{-1}\mathbf{L}_c)^{-1}\hat{\mathbf{r}}, \quad (8)$$

where the hat represents truncating the variables to the quantities related to the tracer field. Interestingly, the elements of \mathbf{w} need not sum to one, nor are they necessarily non-negative, as occurs in linear extrapolation problems. The additional, usually-neglected constant in equation (1),

$$\bar{c}_0 = (\mathbf{c}_0^T\hat{\mathbf{S}}^{-1} + \mathbf{q}^T\mathbf{Q}^{-1}\mathbf{L}_c)(\hat{\mathbf{S}}^{-1} + \hat{\mathbf{E}}^T\mathbf{W}^{-1}\hat{\mathbf{E}} + \mathbf{L}_c^T\mathbf{Q}^{-1}\mathbf{L}_c)^{-1}\hat{\mathbf{r}}, \quad (9)$$

541 is related to the sampling bias. If all the observations have a value of zero, the best
 542 estimate of the global mean has a value of \bar{c}_0 , indicating that prior information is
 543 being used to calculate the global mean. Thus, the degree to which the observa-
 544 tions sample the global ocean in a biased way is quantified. In the case that no
 545 observations are available, \bar{c}_0 reverts to the first-guess global mean. The weights

546 and the constant are optimal in the sense that they solve a tapered, weighted least
547 squares problem.

548 The map of observational weights is spatially heterogeneous with eastern At-
549 lantic points generally having the smallest weights (Figure 8). A point in the
550 Indian Ocean is upweighted the most, with $w \approx 10/N$ (or 10 times the weight
551 that it would be given in the basic arithmetic mean). This map generally corre-
552 sponds to the upweighting of Pacific data points (due to their relative sparsity)
553 and downweighting of Atlantic points. Finer detail is also present, however, such
554 as the upweighting of the few points in the Nordic Seas, but a downweighting of
555 nearby points that are just south of the Greenland-Iceland-Scotland ridge. Other
556 details depend on the flow patterns in the glacial circulation, as observations have
557 influence both up- and downstream.

558 5.2. *Interpreting data histograms*

559 Important information about $\Delta_{\text{MG}}[\overline{\delta^{13}\text{C}_{\text{DIC}}}]$ is available by aggregating point-
560 wise estimates of $\Delta_{\text{MG}}[\delta^{13}\text{C}_{\text{DIC}}]$ in a histogram. Pointwise values of $\Delta_{\text{MG}}[\delta^{13}\text{C}_{\text{DIC}}]$
561 are here inferred by projecting the modern-day state estimate $\delta^{13}\text{C}_{\text{DIC}}$ field onto
562 the core sites by a linear interpolation of the 8 nearest gridpoints, then comparing
563 with LGM sediment core values. In our 492 points of $\Delta_{\text{MG}}[\delta^{13}\text{C}_{\text{DIC}}]$, the median
564 is 0.45‰ and the mean is 0.39‰ (upper left panel Figure 9). The mode of the
565 distribution is 0.6‰, which suggests that Shackleton (1977) was more likely to
566 estimate a number this high with a small number of cores. It is not clear from this
567 analysis, however, whether the mean of the histogram is a good estimate for the
568 global-mean $\delta^{13}\text{C}_{\text{DIC}}$.

To better interpret such a histogram, consider formulating a modern-day and
LGM equation of the type of equation (1) and taking their difference. For a general

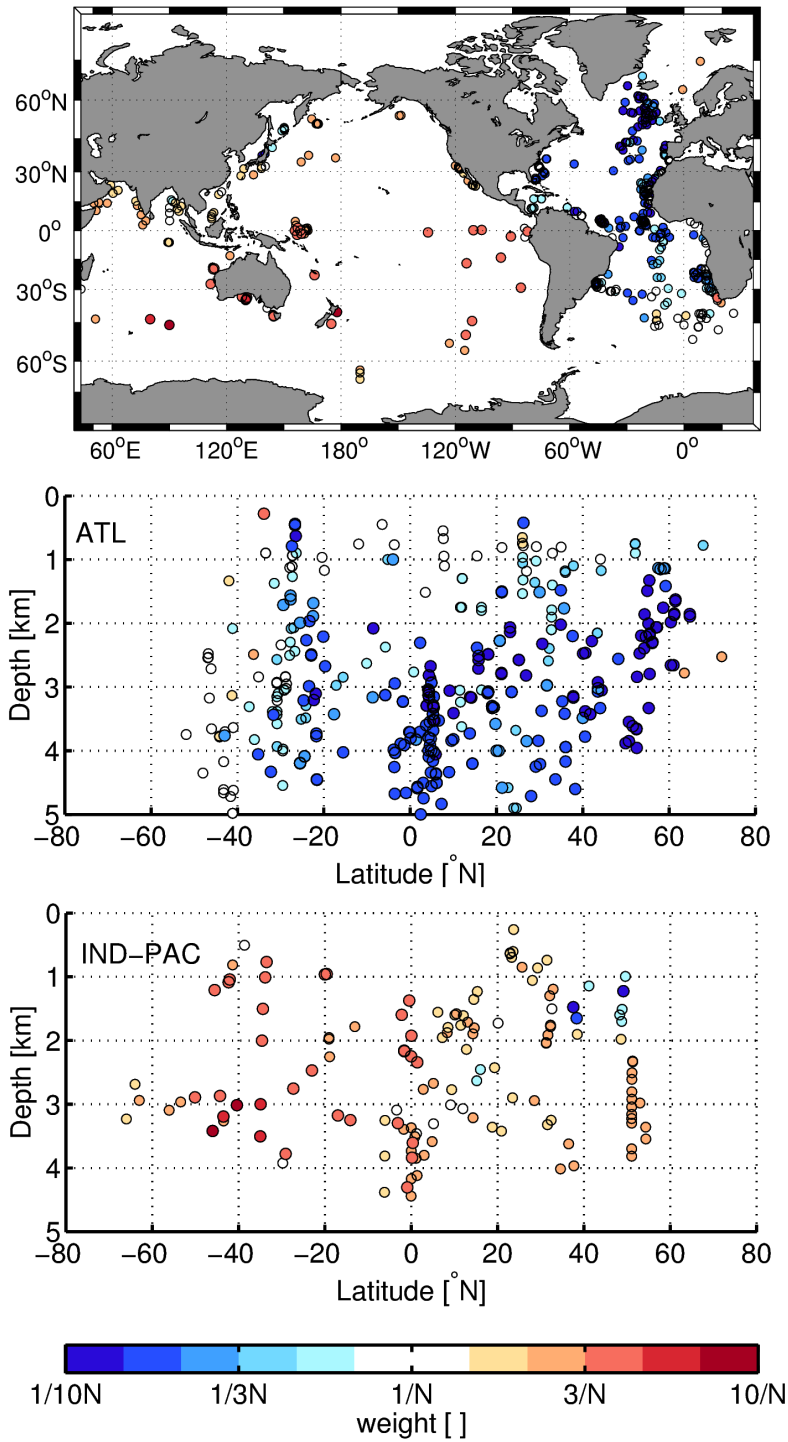


Figure 8: Optimal observational weights to construct a global mean given the glacial circulation (LGM State Estimate 1): plan view (*top*), Atlantic data (*middle*) and Indo-Pacific data (*bottom*). The colorscale is logarithmic. The weights vary from 10 times greater to 100 times lesser than the arithmetic-mean weight and thus some values are offscale low (saturated at a value of $1/10N$).

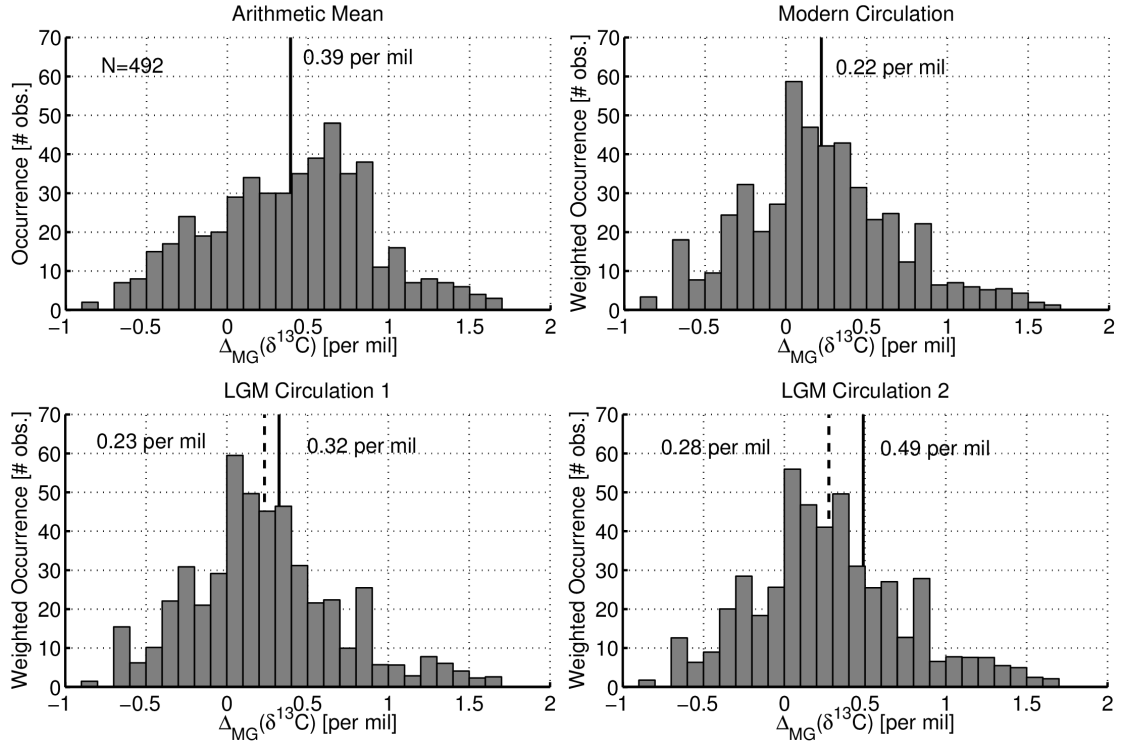


Figure 9: Inference of LGM-to-modern $\delta^{13}C_{DIC}$ change from pointwise measurements. *Upper left:* Histogram of the 492 observations of $\Delta_{MG}[\delta^{13}C_{DIC}]$. *Upper right:* Histogram modified by the optimal weights computed for the modern-day circulation. *Bottom row:* Histogram modified by the optimal weights computed for the glacial circulation (*lower left:* LGM State Estimate 1, *lower right:* LGM State Estimate 2). The inferred $\Delta_{MG}[\delta^{13}C_{DIC}]$ (*solid lines*) results from the mean of the histogram in the top row. In the bottom row, the mean of the histogram (*dashed lines*) is corrected by the last two terms in equation (10) to produce the $\Delta_{MG}[\delta^{13}C_{DIC}]$ estimate (*solid lines*).

tracer, we obtain

$$\Delta_{\text{MG}}(\bar{c}) = \bar{\bar{\mathbf{w}}}^T \Delta_{\text{MG}}(\mathbf{y}) + \Delta_{\text{MG}}(\mathbf{w})^T \bar{\bar{\mathbf{y}}} + \Delta_{\text{MG}}(\bar{c}_0), \quad (10)$$

569 where the Δ_{MG} operator acts elementwise on each vector and the double overbar
570 represents the temporal mean of modern-day and LGM conditions (to distinguish
571 from the single overbar that is a global spatial average). The mean of the aforment-
572 tioned histogram reflects the true global mean in the case that the data weights are
573 based on the arithmetic mean ($\bar{\bar{w}}_i = 1/N$ for all i) and that the second and third
574 terms of equation (10) vanish. As discussed in the Introduction, the spatially ir-
575 regular distribution of observations makes these conditions improbable, and thus
576 the mean of the histogram is not usually a good estimate of global-mean change.

577 When a circulation is available to compute the optimal weights of equation (8)
578 and the constant of equation (9), the mean LGM-to-modern change can be better
579 estimated. For illustration, consider a case where it is assumed that the modern-
580 day circulation is representative of the LGM. Then we can use the calculated
581 modern-day weights (\mathbf{w}_M) to better approximate the first term of equation (10).
582 These weights shift the mode of the distribution to $\Delta_{\text{MG}}[\delta^{13}\text{C}_{\text{DIC}}] = 0.05\text{‰}$ and the
583 inferred global-mean decreases from 0.39‰ to 0.22‰ (visualized as a weighted
584 histogram, upper right panel, Figure 9). In effect, the observations of smaller
585 change are upweighted because they are located along modern-day circulation
586 pathways that influence more of the ocean.

587 A full interpretation of the pointwise data should also account for LGM-to-
588 modern circulation change, of course. In particular, we use both the circulations
589 from LGM State Estimate 1 and 2 (lower row, Figure 9). The mean of the his-
590 togram is again modified, this time back toward larger values (0.23‰ and 0.28‰ ,
591 respectively). The two correction terms due to the changing ocean circulation

592 must also be considered (terms 2 and 3 of the right hand side of equation 10).
593 For LGM State Estimate 1, the correction is 0.09‰ and the final estimate of
594 $\Delta_{\text{MG}}[\overline{\delta^{13}\text{C}_{\text{DIC}}}] = 0.32\text{‰}$ is consistent with the results showcased in Sections 3 and
595 4. For LGM State Estimate 2, the correction is even larger: 0.21‰ (dominated
596 by term 3: 0.15‰). A global-mean change of $\Delta_{\text{MG}}[\overline{\delta^{13}\text{C}_{\text{DIC}}}] = 0.49\text{‰}$ is then diag-
597 nosed from equation (10), smaller than the actual 0.59‰, which is symptomatic
598 of the breakdown of the linear assumption (i.e., equation B.4). Unfortunately, the
599 correction terms are poorly known due to the uncertainty in the LGM circulation.
600 We emphasize that the correction cannot be determined from the data histogram
601 alone.

602 **6. Conclusion**

603 The LGM-to-modern $\delta^{13}\text{C}_{\text{DIC}}$ change is explicitly estimated by first mapping
604 benthic foraminiferal observations onto a global grid, and then taking a mass-
605 weighted average of the gridded values. The mapping process, however, requires a
606 method more sophisticated than typical interpolation because of the sparsity of the
607 dataset and large spatial gaps. Here we demonstrate that an LGM state estimate
608 derived from a recent compilation of 492 $\delta^{13}\text{C}$ data points combined with a tracer
609 transport model can provide a reasonable globally-gridded field, as well as self-
610 consistent uncertainty estimates. Our updated best estimate of LGM-to-modern
611 global $\delta^{13}\text{C}_{\text{DIC}}$ change is $0.32 \pm 0.20\text{‰}$ at the 2σ uncertainty level. A coherent
612 picture of the LGM $\delta^{13}\text{C}$ distribution emerges that is consistent with previous
613 Atlantic estimates and fills in the missing details of the Pacific distribution. Maps
614 of the LGM-to-modern difference in $\delta^{13}\text{C}$ also display coherent spatial patterns,
615 with largest changes in the Atlantic sector of the Southern Ocean.

616 While previous investigators have used various sub-domains and multiple-
617 step averaging techniques to determine how to best weight pointwise observa-
618 tions to obtain the global mean, here we show that determination of the optimal
619 data weights requires knowledge of the ocean circulation. The diagnosed optimal
620 weights conform to expectation in many ways, such as upweighting data in re-
621 gions with sparse coverage. It is very difficult, however, to determine the global
622 mean change from pointwise histograms of the local $\delta^{13}\text{C}_{\text{DIC}}$ change unless the
623 concomitant circulation change is also known. Thus, much of the existing un-
624 certainty in LGM-to-modern $\delta^{13}\text{C}$ change is due to the difficulty in determining
625 the glacial ocean circulation.

626 Our glacial state estimate points toward future directions to reduce the consid-
627 erable remaining global-mean $\delta^{13}\text{C}_{\text{DIC}}$ uncertainty. For example, the addition of
628 randomly-distributed hypothetical data would reduce the uncertainty of the global
629 mean as $N^{-1/2}$, where N is the number of observations. Furthermore, the great-
630 est differences between two LGM estimates that both fit the data occur in the
631 upper ocean, the Southern Ocean, and various marginal seas, pointing to regions
632 where additional information would be most useful. In particular, a compilation
633 of planktonic records would help reduce the uncertainty in surface regions. Pro-
634 vided that challenges with interpretation regarding DIC change and species offsets
635 can be overcome (e.g., Spero et al., 1997), we expect that strategic sampling can
636 reduce the global-mean uncertainty at a faster rate than the hypothetical randomly-
637 sampled case. A two-pronged approach appears best suited to reduce the global-
638 mean uncertainty: compilation of information from strategically-placed locations,
639 including planktonic records, and the implementation of a more sophisticated dy-
640 namical model that can better constrain the circulation for making global maps.

641 **Appendix A. Input variables**

642 The input variables include the weighting matrices for the different constraints
643 of equation (7). The \mathbf{S}^{-1} matrix is chosen to reflect prior knowledge of the $\delta^{13}\text{C}_{\text{DIC}}$
644 field and mass flux ratios. For example, the surface $\delta^{13}\text{C}_{\text{DIC}}$ is assumed to vary by
645 no more than 2.4‰ with lengthscales no smaller than 10° of latitude or longitude
646 (following the nondiagonal weighting matrix method of Gebbie et al. (2006)).
647 The mass flux ratios, \mathbf{m} , are given a prior uncertainty of 0.3 (relative to their
648 nondimensional range of 0 to 1), chosen by the standard deviation of the \mathbf{m} entries
649 for the modern-day circulation. This choice reflects our desire to constrain the
650 glacial circulation with little subjective prior information, but to require that the
651 statistics of glacial transport should not fall outside the range of the modern-day
652 statistics. For the modern-day circulation, on the other hand, we estimate that the
653 uncertainty of the \mathbf{m} values is about 0.05, based on the differences between various
654 modern solutions. The \mathbf{W}^{-1} matrix assumes that the observational uncertainty
655 is 0.2‰, as discussed in the body of the text. The choice of the \mathbf{Q}^{-1} matrix
656 agnostically assumes that the glacial source of remineralized material is the same
657 magnitude as the modern day source or sink.

658 **Appendix B. Uncertainty derivation**

659 *Appendix B.1. Least-squares solution*

Section 2.4 defines a cost function, $J = \mathbf{u}^T \mathbf{S}^{-1} \mathbf{u} + \mathbf{n}^T \mathbf{W}^{-1} \mathbf{n} + \mathbf{v}^T \mathbf{Q}^{-1} \mathbf{v}$, that is
here written in a more complete form by substituting the equations for the first-
guess adjustment, the observational constraint, and the model:

$$J = (\mathbf{x} - \mathbf{x}_0)^T \mathbf{S}^{-1} (\mathbf{x} - \mathbf{x}_0) + (\mathbf{E}\mathbf{x} - \mathbf{y})^T \mathbf{W}^{-1} (\mathbf{E}\mathbf{x} - \mathbf{y}) + (\mathcal{L}[\mathbf{x}] - \mathbf{q})^T \mathbf{Q}^{-1} (\mathcal{L}[\mathbf{x}] - \mathbf{q}). \quad (\text{B.1})$$

The solution, $\tilde{\mathbf{x}}$, is at the minimum of J and thus satisfies the stationary assumption:

$$J_{\tilde{\mathbf{x}}} = 2\{\mathbf{S}^{-1}(\mathbf{x} - \mathbf{x}_0) + \mathbf{E}^T \mathbf{W}^{-1}(\mathbf{E}\mathbf{x} - \mathbf{y}) + \mathbf{L}_{\tilde{\mathbf{x}}}^T \mathbf{Q}^{-1}(\mathcal{L}[\mathbf{x}] - \mathbf{q})\} = 0, \quad (\text{B.2})$$

where $J_{\tilde{\mathbf{x}}} \equiv \partial J / \partial \mathbf{x}|_{\tilde{\mathbf{x}}}$. We define a linearization of model in the neighborhood of the solution:

$$\mathcal{L}[\mathbf{x}] = \mathcal{L}[\mathbf{x}'] + \mathbf{L}_{\mathbf{x}'}(\mathbf{x} - \mathbf{x}') + \varepsilon, \quad (\text{B.3})$$

where ε represents the higher-order terms in the expansion. The solution estimate, $\tilde{\mathbf{x}}$, satisfies

$$\tilde{\mathbf{x}} = (\mathbf{S}^{-1} + \mathbf{E}^T \mathbf{W}^{-1} \mathbf{E} + \mathbf{L}_{\mathbf{x}'}^T \mathbf{Q}^{-1} \mathbf{L}_{\mathbf{x}'})^{-1} \{\mathbf{S}^{-1} \mathbf{x}_0 + \mathbf{E}^T \mathbf{W}^{-1} \mathbf{y} + \mathbf{L}_{\mathbf{x}'}^T \mathbf{Q}^{-1} (\mathbf{q} + \mathbf{L}_{\mathbf{x}'} \mathbf{x}' - \mathcal{L}[\mathbf{x}'])\}, \quad (\text{B.4})$$

660 where the higher-order terms become negligible as one approaches the solution
661 and are dropped from this last equation.

662 *Appendix B.2. Uncertainty of tracer distribution and circulation*

Here we seek the expected solution in the hypothetical case that a perfect first-guess, observations, and tracer source are available (\mathbf{x}_0^* , \mathbf{y}^* , and \mathbf{q}^* , respectively). Defining

$$\mathbf{d}_0 = \mathbf{S}^{-1} \mathbf{x}_0^* + \mathbf{E}^T \mathbf{W}^{-1} \mathbf{y}^* + \mathbf{L}_{\mathbf{x}'}^T \mathbf{Q}^{-1} (\mathbf{q}^* + \mathbf{L}_{\mathbf{x}'} \mathbf{x}' - \mathcal{L}[\mathbf{x}']), \quad (\text{B.5})$$

the expected solution is

$$\langle \tilde{\mathbf{x}} \rangle = (\mathbf{S}^{-1} + \mathbf{E}^T \mathbf{W}^{-1} \mathbf{E} + \mathbf{L}_{\tilde{\mathbf{x}}}^T \mathbf{Q}^{-1} \mathbf{L}_{\tilde{\mathbf{x}}})^{-1} \mathbf{d}_0. \quad (\text{B.6})$$

The dispersion of $\tilde{\mathbf{x}} - \langle \tilde{\mathbf{x}} \rangle$ is equal to the solution covariance of $\tilde{\mathbf{x}}$:

$$\mathbf{C}_{\tilde{\mathbf{x}}} \equiv \langle (\tilde{\mathbf{x}} - \langle \tilde{\mathbf{x}} \rangle) (\tilde{\mathbf{x}} - \langle \tilde{\mathbf{x}} \rangle)^T \rangle, \quad (\text{B.7})$$

and substitution of equation (B.6) into (B.7) gives

$$\mathbf{C}_{\bar{\mathbf{x}}} = (\mathbf{S}^{-1} + \mathbf{E}^T \mathbf{W}^{-1} \mathbf{E} + \mathbf{L}_{\bar{\mathbf{x}}}^T \mathbf{Q}^{-1} \mathbf{L}_{\bar{\mathbf{x}}})^{-1} \langle (\mathbf{d} - \mathbf{d}_0)(\mathbf{d} - \mathbf{d}_0)^T \rangle (\mathbf{S}^{-1} + \mathbf{E}^T \mathbf{W}^{-1} \mathbf{E} + \mathbf{L}_{\bar{\mathbf{x}}}^T \mathbf{Q}^{-1} \mathbf{L}_{\bar{\mathbf{x}}})^{-1}. \quad (\text{B.8})$$

Assuming that errors in the first guess, observations, and model are uncorrelated (i.e., $\mathbf{R}_{xn} = 0$, $\mathbf{R}_{xq} = 0$, etc.), the expected value in the right hand side of (B.8) is

$$\langle (\mathbf{d} - \mathbf{d}_0)(\mathbf{d} - \mathbf{d}_0)^T \rangle = \mathbf{S}^{-1} \mathbf{R}_{xx} \mathbf{S}^{-1} + \mathbf{E}^T \mathbf{W}^{-1} \mathbf{R}_{nn} \mathbf{W}^{-1} \mathbf{E} + \mathbf{L}_{\bar{\mathbf{x}}}^T \mathbf{Q}^{-1} \mathbf{R}_{qq} \mathbf{Q}^{-1} \mathbf{L}_{\bar{\mathbf{x}}}. \quad (\text{B.9})$$

Substituting equation (B.9) into (B.8) and assuming that the weight matrices are equal to the expected second-moment matrices of the residuals (i.e., $\mathbf{R}_{nn} = \mathbf{W}$, $\mathbf{R}_{qq} = \mathbf{Q}$, and $\mathbf{R}_{xx} = \mathbf{S}$), we obtain the solution covariance in terms of the known input variables:

$$\mathbf{C}_{\bar{\mathbf{x}}} = (\mathbf{S}^{-1} + \mathbf{E}^T \mathbf{W}^{-1} \mathbf{E} + \mathbf{L}_{\bar{\mathbf{x}}}^T \mathbf{Q}^{-1} \mathbf{L}_{\bar{\mathbf{x}}})^{-1}, \quad (\text{B.10})$$

663 that is used in the main text as equation (6). The standard error is here defined as
664 $\pm \sqrt{\mathbf{C}_{\bar{\mathbf{x}}}}$ of the diagonal elements.

665 **Appendix C. Calculation of the optimal observational weights**

In the case that the circulation is known exactly, the cost function equation (B.1) can be simplified

$$J = (\mathbf{c} - \mathbf{c}_0)^T \hat{\mathbf{S}}^{-1} (\mathbf{c} - \mathbf{c}_0) + (\hat{\mathbf{E}}\mathbf{c} - \mathbf{y})^T \mathbf{W}^{-1} (\hat{\mathbf{E}}\mathbf{c} - \mathbf{y}) + (\mathbf{L}_c \mathbf{c} - \mathbf{q})^T \mathbf{Q}^{-1} (\mathbf{L}_c \mathbf{c} - \mathbf{q}), \quad (\text{C.1})$$

where the hat indicates truncation of the \mathbf{E} and \mathbf{S} matrices to the parts related to the tracer field. Using the least-squares estimate of the tracer solution and the following definition of the global mean, $\bar{c} = \hat{\mathbf{f}}^T \mathbf{c}$, where $\hat{\mathbf{f}}$ is also a truncated vector,

we obtain a simplified equation

$$\tilde{\mathbf{c}} = \hat{\mathbf{r}}^T (\hat{\mathbf{S}}^{-1} + \hat{\mathbf{E}}^T \mathbf{W}^{-1} \hat{\mathbf{E}} + \mathbf{L}_c^T \mathbf{Q}^{-1} \mathbf{L}_c)^{-1} (\hat{\mathbf{S}}^{-1} \mathbf{c}_0 + \hat{\mathbf{E}}^T \mathbf{W}^{-1} \mathbf{y} + \mathbf{L}_c^T \mathbf{Q}^{-1} \mathbf{q}). \quad (\text{C.2})$$

Comparison of the equation (C.2) to equation (1) permits the identification of the optimal data weights:

$$\mathbf{w} = \mathbf{W}^{-1} \hat{\mathbf{E}} (\hat{\mathbf{S}}^{-1} + \hat{\mathbf{E}}^T \mathbf{W}^{-1} \hat{\mathbf{E}} + \mathbf{L}_c^T \mathbf{Q}^{-1} \mathbf{L}_c)^{-1} \hat{\mathbf{r}}, \quad (\text{C.3})$$

and the additional constant

$$\bar{c}_0 = (\mathbf{c}_0^T \hat{\mathbf{S}}^{-1} + \mathbf{q}^T \mathbf{Q}^{-1} \mathbf{L}_c) (\hat{\mathbf{S}}^{-1} + \hat{\mathbf{E}}^T \mathbf{W}^{-1} \hat{\mathbf{E}} + \mathbf{L}_c^T \mathbf{Q}^{-1} \mathbf{L}_c)^{-1} \hat{\mathbf{r}}. \quad (\text{C.4})$$

666 Acknowledgments

667 The authors are indebted to Olivier Marchal for thoroughly commenting on a ver-
 668 sion of the manuscript and the mathematics. The authors thank Ed Boyle, Thomas
 669 Chalk, David McGee, and Alan Mix for helpful discussions. GG is supported
 670 by NSF grants OIA-1124880 and OCE-1357121, the WHOI Ocean and Climate
 671 Change Institute, and The Joint Initiative Awards Fund from the Andrew W. Mel-
 672 lon Foundation.

673

674 References

675 Adams, J. M., Faure, H., 1998. A new estimate of changing carbon storage on
 676 land since the Last Glacial Maximum, based on global land ecosystem recon-
 677 struction. *Global and Planetary Change* 16, 3–24.

678 Adkins, J., McIntyre, K., Schrag, D., 2002. The salinity, temperature, and $\delta^{18}\text{O}$ of
 679 the glacial deep ocean. *Science* 298, 1724–1725.

- 680 Arbic, B. K., MacAyeal, D. R., Mitrovica, J. X., Milne, G. A., 2004. Palaeocli-
681 mate: Ocean tides and Heinrich events. *Nature* 432 (7016), 460–460.
- 682 Boyle, E. A., 1992. Cadmium and $\delta^{13}\text{C}$ paleochemical ocean distributions during
683 the Stage 2 Glacial Maximum. *Annual Review of Earth and Planetary Sciences*
684 20 (1), 245–287.
- 685 Bretherton, F., Davis, R., Fandry, C., 1976. A technique for objective analysis and
686 design of oceanographic experiments applied to MODE-73. *Deep-Sea Res* 23,
687 559–582.
- 688 Broecker, W., Maier-Reimer, E., 1992. The influence of air and sea exchange on
689 the carbon isotope distribution in the sea. *Global Biogeochemical Cycles* 6 (3),
690 315–320.
- 691 Broecker, W., McGee, D., 2013. The ^{13}C record for atmospheric CO_2 : What is it
692 trying to tell us? *Earth and Planetary Science Letters* 368, 175–182.
- 693 Ciais, P., Tagliabue, A., Cuntz, M., Bopp, L., Scholze, M., Hoffmann, G., Loran-
694 tou, A., Harrison, S., Prentice, I., Kelley, D., et al., 2012. Large inert carbon
695 pool in the terrestrial biosphere during the Last Glacial Maximum. *Nature Geo-
696 science* 5 (1), 74–79.
- 697 Crowley, T. J., 1995. Ice age terrestrial carbon changes revisited. *Global Biogeo-
698 chemical Cycles* 9 (3), 377–389.
- 699 Curry, W., Duplessy, J., Labeyrie, L., Shackleton, N., 1988. Changes in the
700 distribution of $\delta^{13}\text{C}$ of deep water ΣCO_2 between the last glaciation and the
701 Holocene. *Paleoceanography* 3 (3).

- 702 Curry, W., Oppo, D., 2005. Glacial water mass geometry and the distribu-
703 tion of $\delta^{13}\text{C}$ of ΣCO_2 in the Western Atlantic Ocean. *Paleoceanography* 20,
704 10.1029/2004PA001021.
- 705 Duplessy, J., Shackleton, N., Fairbanks, R., Labeyrie, L., Oppo, D., Kallel, N.,
706 1988. Deepwater source variations during the last climatic cycle and their im-
707 pact on the global deepwater circulation. *Paleoceanography* 3 (3).
- 708 Duplessy, J., Shackleton, N., Matthews, R., Prell, W., Ruddiman, W., Caralp,
709 M., Hendy, C., 1984. ^{13}C record of benthic foraminifera in the last interglacial
710 ocean: Implications for the carbon cycle and the global deep water circulation.
711 *Quaternary Research* 21 (2), 225–243.
- 712 Gebbie, G., 2014. How much did Glacial North Atlantic Water shoal? *Paleo-*
713 *ceanography* 29 (3), 190–209.
- 714 Gebbie, G., Heimbach, P., Wunsch, C., 2006. Strategies for Nested
715 and Eddy-Permitting State Estimation. *J. Geophys. Res.* 111, C10073,
716 10.1029/2005JC003094.
- 717 Gebbie, G., Huybers, P., 2010. Total matrix intercomparison: a method for re-
718 solving the geometry of water-mass pathways. *J. Phys. Oceanogr.* 40 (8), 1710–
719 1728, DOI: 10.1175/2010JPO4272.1.
- 720 Gebbie, G., Huybers, P., 2012. The mean age of ocean waters inferred from radio-
721 carbon observations: sensitivity to surface sources and accounting for mixing
722 histories. *J. Phys. Oceanogr.* 42 (2), DOI: 10.1175/JPO-D-11-043.1, 291–305.
- 723 Gruber, N., Keeling, C. D., Bacastow, R. B., Guenther, P. R., Lueker, T. J., Wahlen,
724 M., Meijer, H. A., Mook, W. G., Stocker, T. F., 1999. Spatiotemporal patterns

- 725 of carbon-13 in the global surface oceans and the oceanic Suess effect. *Global*
726 *Biogeochemical Cycles* 13 (2), 307–335.
- 727 Herguera, J., Herbert, T., Kashgarian, M., Charles, C., 2010. Intermediate and
728 deep water mass distribution in the Pacific during the Last Glacial Maximum
729 inferred from oxygen and carbon stable isotopes. *Quaternary Science Reviews*
730 29 (9), 1228–1245.
- 731 Hesse, T., Butzin, M., Bickert, T., Lohmann, G., 2011. A model-data compari-
732 son of $\delta^{13}\text{C}$ in the glacial Atlantic Ocean. *Paleoceanography*, 26, PA3220. 26,
733 PA3220.
- 734 Hesse, T., Wolf-Gladrow, D., Lohmann, G., Bijma, J., Mackensen, A., Zeebe,
735 R. E., 2014. Modelling $\delta^{13}\text{C}$ in benthic foraminifera: Insights from model sen-
736 sitivity experiments. *Marine Micropaleontology* 112, 50–61.
- 737 Hide, R., 1969. Dynamics of the atmospheres of the major planets with an ap-
738 pendix on the viscous boundary layer at the rigid bounding surface of an
739 electrically-conducting rotating fluid in the presence of a magnetic field. *J. At-*
740 *mos. Sci.* 26, 841–853.
- 741 IOC, S., 2010. IAPSO: The international thermodynamic equation of seawater–
742 2010: Calculation and use of thermodynamic properties, intergovernmental
743 oceanographic commission, manuals and guides no. 56.
- 744 Kaplan, J. O., Prentice, I. C., Knorr, W., Valdes, P. J., 2002. Modeling the dynam-
745 ics of terrestrial carbon storage since the Last Glacial Maximum. *Geophysical*
746 *Research Letters* 29 (22), 31–1.

- 747 Köhler, P., Fischer, H., Schmitt, J., 2010. Atmospheric $\delta^{13}\text{CO}_2$ and its relation
748 to $p\text{CO}_2$ and deep ocean $\delta^{13}\text{C}$ during the late Pleistocene. *Paleoceanography*
749 25 (1).
- 750 Mackensen, A., Schumacher, S., Radke, J., Schmidt, D., 2000. Microhabitat pref-
751 erences and stable carbon isotopes of endobenthic foraminifera: clue to quan-
752 titative reconstruction of oceanic new production? *Marine Micropaleontology*
753 40 (3), 233–258.
- 754 Makou, M. C., Oppo, D. W., Curry, W. B., 2010. South Atlantic intermediate
755 water mass geometry for the Last Glacial Maximum from foraminiferal Cd/Ca.
756 *Paleoceanography* 25 (4).
- 757 Marchal, O., Curry, W., 2008. On the abyssal circulation in the glacial Atlantic.
758 *Journal of Physical Oceanography* 38 (9), 2014–2037.
- 759 Matsumoto, K., Lynch-Stieglitz, J., 1999. Similar glacial and Holocene deep wa-
760 ter circulation inferred from Southeast Pacific benthic foraminiferal carbon iso-
761 tope composition. *Paleoceanography* 14 (2), 149–163.
- 762 Matsumoto, K., Oba, T., Lynch-Stieglitz, J., Yamamoto, H., 2002. Interior hydrog-
763 raphy and circulation of the glacial Pacific Ocean. *Quaternary science reviews*
764 21 (14-15), 1693–1704.
- 765 Monnin, E., Indermuhle, A., Dallenbach, A., Fluckiger, J., Stauffer, B., Stocker,
766 T. F., Raynaud, D., Barnola, J., 2001. Atmospheric CO_2 concentrations over the
767 last glacial termination. *Science* 291, 112–114.

- 768 Nocedal, J., 1980. Updating quasi-Newton matrices with limited storage. *Mathematics of computation* 35 (151), 773–782.
769
- 770 Oliver, K., Hoogakker, B., Crowhurst, S., Henderson, G., Rickaby, R., Edwards,
771 N., Elderfield, H., 2010. A synthesis of marine sediment core $\delta^{13}\text{C}$ data over the
772 last 150 000 years. *Climate of the Past* 6, 645–673.
- 773 Olsen, A., Abdirahman, O., Bellerby, R., Johannessen, T., Ninnemann, U., Brown,
774 K., Olsson, K., Olafsson, J., Nondal, G., Kivimäe, C., et al., 2006. Magnitude
775 and origin of the anthropogenic CO_2 increase and the ^{13}C Suess Effect in the
776 Nordic Seas since 1981.
- 777 Oppo, D. W., McManus, J. F., Cullen, J. L., 2003. Palaeo-oceanography: Deep-
778 water variability in the Holocene epoch. *Nature* 422 (6929), 277–277.
- 779 Peeters, F. J., Brummer, G.-J. A., Ganssen, G., 2002. The effect of upwelling on
780 the distribution and stable isotope composition of *Globigerina bulloides* and
781 *Globigerinoides ruber* (planktic foraminifera) in modern surface waters of the
782 NW Arabian Sea. *Global and Planetary Change* 34 (3), 269–291.
- 783 Peterson, C. D., Lisiecki, L. E., Stern, J. V., 2014. Deglacial whole-ocean $\delta^{13}\text{C}$
784 change estimated from 480 benthic foraminiferal records. *Paleoceanography*.
- 785 Russell, A. D., Spero, H. J., 2000. Field examination of the oceanic carbonate ion
786 effect on stable isotopes in planktonic foraminifera. *Paleoceanography* 15 (1),
787 43–52.
- 788 Schmittner, A., Green, J., Wilmes, S., 2015. Glacial ocean over-turning intensified
789 by tidal mixing in a global circulation model. *Geophys. Res. Lett* 42, 2.

- 790 Schmittner, A., Gruber, N., Mix, A. C., Key, R. M., Tagliabue, A., Westberry,
791 T. K., 2013. Biology and air-sea gas exchange controls on the distribution of
792 carbon isotope ratios ($\delta^{13}\text{C}$) in the ocean. *Biogeosciences Discussions* 10 (5),
793 8415–8466.
- 794 Shackleton, N., 1977. Carbon 13 in Uvigerina: Tropical rainforest history and the
795 equatorial Pacific carbonate dissolution cycles. *Marine science*.
- 796 Spero, H. J., Bijma, J., Lea, D. W., Bemis, B. E., 1997. Effect of seawater
797 carbonate concentration on foraminiferal carbon and oxygen isotopes. *Nature*
798 390 (6659), 497–500.
- 799 Stern, J. V., Lisiecki, L. E., 2014. Termination 1 timing in radiocarbon-dated re-
800 gional benthic $\delta^{18}\text{O}$ stacks. *Paleoceanography*.
- 801 Tagliabue, A., Bopp, L., 2008. Towards understanding global variability in ocean
802 carbon-13. *Global Biogeochemical Cycles* 22 (1).
- 803 Tagliabue, A., Bopp, L., Roche, D., Bouttes, N., Dutay, J., Alkama, R., Kageyama,
804 M., Michel, E., Paillard, D., 2009. Quantifying the roles of ocean circulation
805 and biogeochemistry in governing ocean carbon-13 and atmospheric carbon
806 dioxide at the Last Glacial Maximum. *Clim. Past* 5, 695–706.
- 807 Walker, J. C. G., 1991. *Numerical adventures with geochemical cycles*. Oxford
808 University Press New York.
- 809 Wunsch, C., 1996. *The Ocean Circulation Inverse Problem*. Cambridge University
810 Press.

- 811 Wunsch, C., 2003. Determining paleoceanographic circulations, with emphasis
812 on the Last Glacial Maximum. *Quaternary Science Reviews* 22 (2-4), 371–385.
- 813 Wunsch, C., Ponte, R., Heimbach, P., 2007. Decadal trends in sea level patterns:
814 1993-2004. *Journal of Climate* 20 (24), 5889–5911.